# Structural Mechanism for Modulation of Synaptic Neuroligin-Neurexin Signaling by MDGA Proteins

## Highlights

- The MDGA1 extracellular region has an unusual triangular multi-domain arrangement

- The NL1-MDGA1 complex structure reveals how MDGA proteins block neurexin binding

- MDGA1 and MDGA2 bind all NL isoforms, a process fine-tuned by alternative splicing

- MDGA1 and MDGA2 suppress NL synaptogenic activity in a concentration-dependent manner

## Authors

Jonathan Elegheert,
Vedrana Cvetkovska,
Amber J. Clayton, ..., Jo Begbie,
Ann Marie Craig, A. Radu Aricescu

## Correspondence

jelegheert@strubi.ox.ac.uk (J.E.),
acraig@mail.ubc.ca (A.M.C.),
radu@mrc-lmb.cam.ac.uk (A.R.A.)

## In Brief

Elegheert et al. present the crystal structure of the autism-linked post-synaptic protein MDGA in complex with the synapse organizer neuroligin, providing a structural and mechanistic basis for potentially brain-wide modulation of synaptic neuroligin-neurexin signaling by MDGA proteins.

CrossMark

**Cell**Press

# Structural Mechanism for Modulation of Synaptic Neuroligin-Neurexin Signaling by MDGA Proteins

Jonathan Elegheert,[1,*] Vedrana Cvetkovska,[2] Amber J. Clayton,[1,9] Christina Heroven,[1,3] Kristel M. Vennekens,[4,5] Samuel N. Smukowski,[6] Michael C. Regan,[7] Wanyi Jia,[1,10] Alexandra C. Smith,[8] Hiro Furukawa,[7] Jeffrey N. Savas,[6] Joris de Wit,[4,5] Jo Begbie,[8] Ann Marie Craig,[2,*] and A. Radu Aricescu[1,3,11,*]

[1]Division of Structural Biology, Wellcome Trust Centre for Human Genetics, University of Oxford, Roosevelt Drive, Oxford OX3 7BN, UK
[2]Djavad Mowafaghian Centre for Brain Health and Department of Psychiatry, University of British Columbia, Vancouver, BC V6T 2B5, Canada
[3]MRC Laboratory of Molecular Biology, Francis Crick Avenue, Cambridge Biomedical Campus, Cambridge CB2 0QH, UK
[4]VIB Center for Brain and Disease Research, Herestraat 49, B-3000 Leuven, Belgium
[5]Department of Neurosciences, KU Leuven, Herestraat 49, B-3000 Leuven, Belgium
[6]Department of Neurology, Feinberg School of Medicine, Northwestern University, Chicago, IL 60611, USA
[7]Keck Structural Biology Laboratory, Cold Spring Harbor Laboratory, Cold Spring Harbor, New York, USA
[8]Department of Physiology, Anatomy and Genetics, University of Oxford, South Parks Road, Oxford OX1 3QX, UK
[9]Present Address: Adaptimmune, 60 Jubilee Avenue, Milton Park, Abingdon OX14 4RX, UK
[10]Present Address: Wellcome Trust-Medical Research Council Cambridge Stem Cell Institute, University of Cambridge, Cambridge, UK
[11]Lead Contact
*Correspondence: jelegheert@strubi.ox.ac.uk (J.E.), acraig@mail.ubc.ca (A.M.C.), radu@mrc-lmb.cam.ac.uk (A.R.A.)
http://dx.doi.org/10.1016/j.neuron.2017.07.040

## SUMMARY

Neuroligin-neurexin (NL-NRX) complexes are fundamental synaptic organizers in the central nervous system. An accurate spatial and temporal control of NL-NRX signaling is crucial to balance excitatory and inhibitory neurotransmission, and perturbations are linked with neurodevelopmental and psychiatric disorders. MDGA proteins bind NLs and control their function and interaction with NRXs via unknown mechanisms. Here, we report crystal structures of MDGA1, the NL1-MDGA1 complex, and a spliced NL1 isoform. Two large, multi-domain MDGA molecules fold into rigid triangular structures, cradling a dimeric NL to prevent NRX binding. Structural analyses guided the discovery of a broad, splicing-modulated interaction network between MDGA and NL family members and helped rationalize the impact of autism-linked mutations. We demonstrate that expression levels largely determine whether MDGAs act selectively or suppress the synapse organizing function of multiple NLs. These results illustrate a potentially brain-wide regulatory mechanism for NL-NRX signaling modulation.

## INTRODUCTION

Cell-surface synaptic organizing proteins play a central role in the assembly, maturation, stabilization, and plasticity of neuronal synapses (Siddiqui and Craig, 2011). Members of the presynaptic neurexin (NRX) and postsynaptic neuroligin (NL) transmembrane protein families form the axis of a signaling pathway that is crucial for the formation and function of excitatory and inhibitory synapses throughout the brain (Südhof, 2008). The NL-NRX complexes promote synaptic cell adhesion via direct extracellular interactions and recruit the molecular machinery for neurotransmitter release and reception. NLs recruit ionotropic glutamate and $GABA_A$ receptors through direct interactions or using DLG (Discs large) family or gephyrin and collybistin accessory proteins, respectively (Bemben et al., 2015). NRXs interact intracellularly with CASK and Mint PDZ domain proteins and the synaptic vesicle protein synaptotagmin; α-NRXs also functionally link to presynaptic voltage-gated $Ca^{2+}$ channels (Reissner et al., 2013).

NLs are generated from five genes in humans or four genes in mice, and further diversified by two sites of alternative splicing: spliced sequences A (SSA) and B (SSB). Mammalian NRXs show even greater diversity: over a thousand variants are generated from three genes, two promoters (α and β), and six sites of alternative splicing (SS1–6) (Schreiner et al., 2014; Ullrich et al., 1995). The extracellular region of the NLs contains a cholinesterase-like domain that forms a stable interaction with the α/β-NRX1-3 LNS6 (laminin, NRX, sex-hormone-binding globulin) domain (Araç et al., 2007; Chen et al., 2008; Fabrichny et al., 2007). NL1(+B) binds only β-NRXs (Boucard et al., 2005) and functions at glutamatergic synapses (Song et al., 1999), while NL2 binds all NRXs and functions at GABAergic synapses (Graf et al., 2004; Varoqueaux et al., 2004).

Besides NLs, the various NRXs bind a multitude of postsynaptic protein families to organize synapses: leucine-rich repeat transmembrane proteins (LRRTMs), calsyntenin 3, dystroglycan, latrophilin 1, cerebellins (reviewed in de Wit and Ghosh, 2016), and recently, C1q-like proteins (Matsuda et al., 2016). Molecular interactions are controlled by NRX promoter usage and splicing. For example, introduction of the 30-residue SS4 into β-NRX1 substantially weakens the NL-NRX1 interaction (Koehnke et al., 2010), abolishes the LRRTM1-2-NRX1 interaction (Siddiqui et al., 2010), and directs β-NRX1 into the cerebellin pathway (Elegheert et al., 2016; Uemura et al., 2010). Likewise, alternative binding partners for NL have been recognized. Thrombospondin

1 (TSP1) (Xu et al., 2010) and the NMDA receptor (NMDAR) (Budreck et al., 2013) both bind NL1, and the astrocyte-secreted protein hevin bridges NL1 and α-NRX (Singh et al., 2016) to promote glutamatergic synaptogenesis.

In contrast to all these positive effectors and modulators, the discovery of the Ig superfamily (IgSF) MDGA (meprin, A-5 protein, and receptor protein-tyrosine phosphatase mu [MAM] domain-containing glycosylphosphatidylinositol anchor) proteins as negative modulators of NL is remarkable. MDGA1 was found to block the interaction of NL2 with NRX and suppress inhibitory synapse development in cultured neurons (Pettem et al., 2013), while MDGA2 blocks the interaction of NL1 and NL2 with NRX and can suppress excitatory and inhibitory synapse development (Connor et al., 2016). MDGA proteins are attached to the postsynaptic membrane via a C-terminal GPI anchor, and their large (~900 amino acids) extracellular domain consists of six immunoglobulin-like domains ($Ig_{1-6}$), a fibronectin type III-like ($FnIII_7$) domain, and a memprin, A5, mu ($MAM_8$) domain.

Aberrant signaling in the NL-NRX pathway is strongly linked to autism spectrum disorders (ASDs) and schizophrenia (Südhof, 2008). Similarly, intronic SNPs in *MDGA1* are linked to schizophrenia (Kähler et al., 2008; Li et al., 2011), and *MDGA2* loss-of-function truncations were found in unrelated cases of ASD (Bucan et al., 2009). Single-allele knockout of the *Mdga2* gene in mice elevated both excitatory neurotransmission and functional connectivity and produced behavioral phenotypes related to ASD (Connor et al., 2016). *Mdga2* haploinsufficiency phenotypes were associated with elevated levels of NL1 and DLG family proteins and proposed to be due to diminished block of NL1-NRX signaling (Connor et al., 2016). However, based on a novel synaptic cleft tagging strategy in cell culture, another recent study proposed a role for MDGA2 selectively at inhibitory synapses and MDGA1 at excitatory synapses (Loh et al., 2016), raising controversy about the precise functions of MDGAs and revealing a need for more in-depth comprehensive analyses.

Despite the recent focus on mapping the complex molecular landscape of NL-NRX signaling modulators, a structural and mechanistic understanding of these processes is still lacking. In this study, we present the crystal structure of the near-complete MDGA1 extracellular domain and that of its prototypical complex with NL1, providing detailed insight into the structural basis of the modulation of NL-NRX signaling by MDGA proteins. We show that human MDGA1 and MDGA2 have the ability to interact with human NL1–5, thereby extending the previously proposed restricted, binary NL-MDGA interaction code (Connor et al., 2016; Lee et al., 2013; Pettem et al., 2013). Furthermore, we demonstrate that MDGA1 and MDGA2 are able to broadly block NL synaptogenic activity in a concentration- and splice insert-dependent fashion. Given the broad distribution of MDGA and NL-NRX complexes, our work provides a framework for understanding potential brain-wide modulation of NL-NRX signaling by MDGA proteins.

## RESULTS

### Crystal and Solution Structure of MDGA1

As a first step toward solving the structure of an NL-MDGA complex, we targeted the full-length apo MDGA1 extracellular domain for crystallization. Following an extensive screen of constructs from various species, we obtained diffraction-quality crystals and solved the structure of the complete chicken MDGA1 extracellular region ($cMDGA1_{ECTO}$; $Ig_1$-$Mam_8$; Gln19-Lys919; 79.5% sequence identity and 88.4% sequence similarity with human $MDGA1_{ECTO}$; Figure S1) using selenomethionine single-wavelength anomalous diffraction (Se-SAD) at 3.20 Å (Figures 1A and 1B; Table S1). $cMDGA1_{ECTO}$ was treated with endo-glycosidase F1 (Endo F1) prior to crystallization, leaving a single N-linked *N*-acetylglucosamine monosaccharide on glycosylated Asn residues after enzymatic cleavage. Seven domains ($Ig_{1-6}$ to $FnIII_7$) could be unequivocally resolved in the electron density maps; however, the C-terminal $MAM_8$ domain was not visible and most likely highly mobile and accommodated in the solvent channels of the crystal. The $cMDGA1_{ECTO}$ $Ig_{1-6}$-$FnIII_7$ domains form a surprisingly compact, folded structure that is ~120 Å wide, ~110 Å high, and ~50 Å deep, fitting comfortably within the typical height of the synaptic cleft (~20–25 nm). Its approximately triangular shape, unique among the cell-surface receptors crystallized to date, is a consequence of sharp-angled $Ig_2$-$Ig_3$, $Ig_4$-$Ig_5$, and $Ig_6$-$FnIII_7$ inter-domain linkers that are stabilized by numerous inter-domain contacts.

The $Ig_2$-$Ig_3$ domain contacts (341 Å$^2$ buried surface area [BSA]) are formed between (1) the $Ig_2$ β strands βA and βG and (2) the loop structure connecting $Ig_2$ and $Ig_3$, and also $Ig_3$ loops *BC* and *FG*. The $Ig_4$-$Ig_5$ domain contacts (598 Å$^2$ BSA) are formed between (1) the $Ig_4$ β strand βA and loop *AB* and (2) $Ig_5$ loops *BC* and *FG*. The $Ig_6$-$FnIII_7$ domain contacts (396 Å$^2$ BSA) are formed between (1) the Ig6 β strand βA′ and loops *A′B* and *EF* and (2) the loop connecting $Ig_6$ and $FnIII_7$ and $FnIII_7$ loops *BC* and *FG*. Finally, the $Ig_1$-$FnIII_7$ domain contacts (395 Å$^2$ BSA) close the $cMDGA1_{ECTO}$ triangle and are formed between (1) the $Ig_1$ N-terminal stretch (Gln19-Tyr22) and loop *BC* and (2) $FnIII_7$ loops *AA′* and *C′E*, and β strands βA and βB (Figure 1C). The linear orientation of $Ig_1$ and $Ig_2$ is stabilized by a disulfide bond, distinct from the core Ig domain disulfide bonds, between Cys36 located on $Ig_1$ loop *AA′* and Cys222 located on $Ig_2$ loop *FG* (Figures 1A and 1B).

In the crystal, two MDGA molecules form an unexpected intertwined dimeric arrangement with individual C-terminal ends pointing in opposite directions (Figure S2A). Homophilic interfaces are formed between domain pairs $Ig_1$-$Ig_5$*, $Ig_2$-$Ig_2$*, and $Ig_6$-$FnIII_7$* (where * denotes contributions from the second MDGA monomer); their combined BSA is 2,666 Å$^2$, suggesting a stable association. Interestingly, this arrangement is compatible with both a potential *cis*- or *trans*-homophilic interaction and might indicate formation of an adhesive or self-inhibitory complex (Figure S2B). Recombinantly expressed MDGA1 targets to axons and dendrites and partially co-localizes with inhibitory and excitatory postsynaptic markers in cultured hippocampal rodent neurons (Loh et al., 2016; Pettem et al., 2013). Native MDGA1 and MDGA2 were observed in axon tracts in chicken (Fujimura et al., 2006) and zebrafish (Ingold et al., 2015), and a putative *trans*-homophilic interaction of MDGA2 was proposed to function in directed axonal growth (Joset et al., 2011).

To investigate the dimerization potential of the MDGA1 extracellular region in solution, we pursued multiple experimental avenues. First, we determined the $cMDGA1_{ECTO}$ solution structure
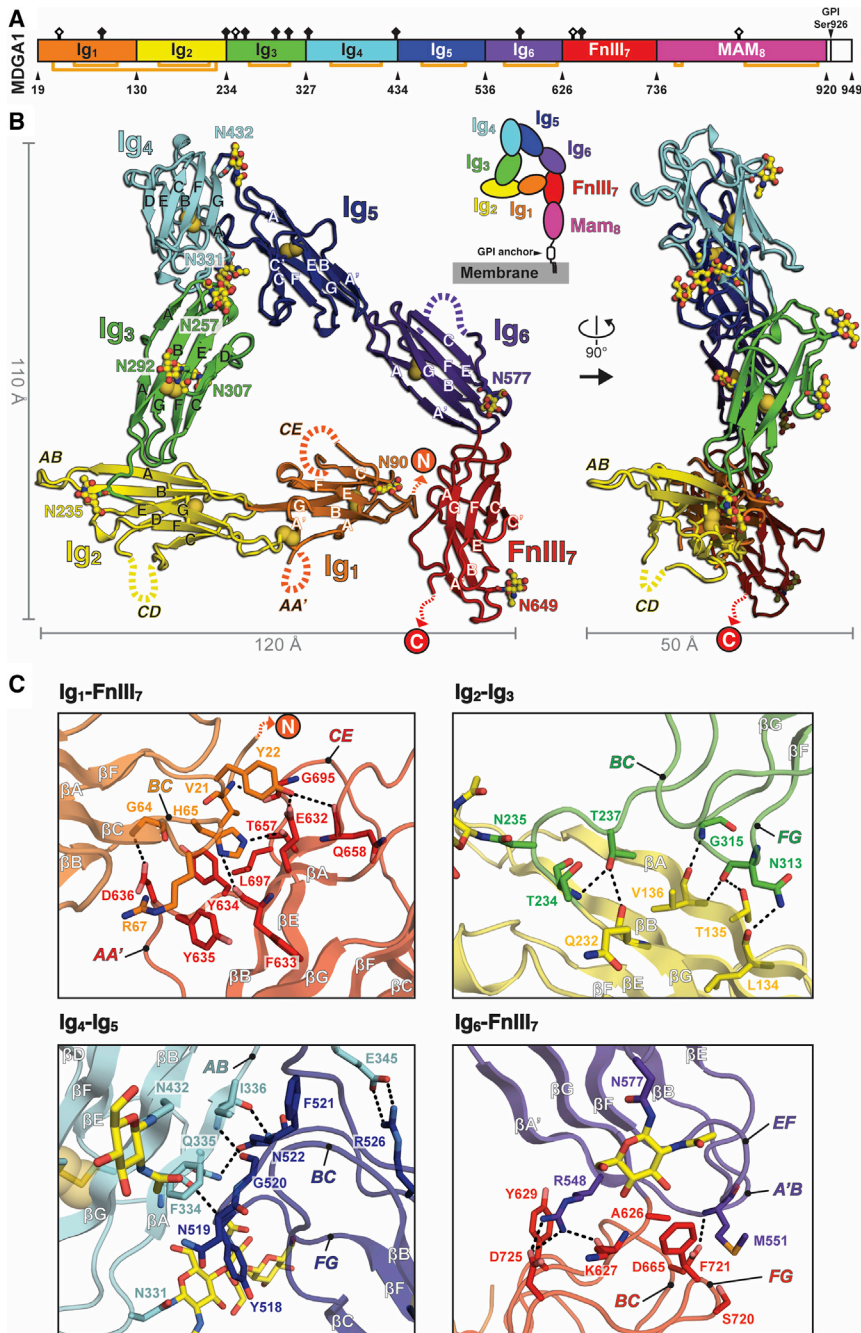
**Figure 1. Crystal Structure of MDGA1**

(A) Schematic representation of the chicken MDGA1 (cMDGA1) domain structure. Gln19-Lys919, spanning $Ig_1$-$Mam_8$, was used for structure determination. Black diamonds indicate Asn residues with crystallographically confirmed N-linked glycosylation (nine positions). Open diamonds indicate Asn residues with predicted but crystallographically unconfirmed N-linked glycosylation (four positions). Orange lines connect cysteine residues engaged in disulfide bonds.

(B) Crystal structure of $cMDGA1_{ECTO}$. Disulfide bridges are shown as yellow spheres. Glycan moieties visible in the electron density maps are shown in ball and stick representation. N and C termini, β strands, and selected $Ig_{1-2}$ loop structures are annotated to the structure. The $MAM_8$ domain was not visible in the electron density maps, probably due to a flexible $FnIII_7$-$Mam_8$ linker.

(C) Details of the $cMDGA1_{ECTO}$ $Ig_1$-$FnIII_7$, $Ig_2$-$Ig_3$, $Ig_4$-$Ig_5$, and $Ig_6$-$FnIII_7$ domain contacts. Putative hydrogen bonds and hydrophilic interactions are indicated with black dashed lines.

See also Figures S1 and S2.

$cMDGA1_{ECTO}$ was compared with a negative control mutant that contained three N-linked glycans inserted at distinct homophilic interfaces (Arg156Asn in $Ig_2$, Ser502Asn in $Ig_5$, and Arg680Asn in $FnIII_7$) for binding to wild-type $cMDGA1_{ECTO}$. Both $cMDGA1_{ECTO}$ variants failed to interact with wild-type $cMDGA1_{ECTO}$ up to a concentration of 100 μM (Figure S2F), indicating that no homophilic $cMDGA1_{ECTO}$ interactions occurred. Together, our results provide no biochemical evidence for an MDGA1 *cis*- or *trans*-homophilic dimer, and we propose that opening of the triangular $cMDGA1_{ECTO}$ structure by transient disruption of the limited $Ig_1$-$FnIII_7$ interface allowed formation of the dimeric arrangement in the crystal lattice.

## Crystal Structure of an NL-MDGA Complex

We performed an extensive crystallization screening of the NL-MDGA complexes formed between $MDGA1$-$2_{ECTO}$ and $NL1$-$2_{ECTO}$ constructs from various species, and succeeded in generating diffraction-quality crystals and determining the structure of the Endo F1-treated complex formed between $cMDGA1_{ECTO}$ and the human NL1 cholinesterase domain lacking splice inserts ($hNL1_{ECTO}$; Gln46-Asp635; Figure S3) at 3.30 Å (Figures 2A and 2B; Table S1). The $hNL1_{ECTO}$-$cMDGA1_{ECTO}$ complex has a 2:2 stoichiometry and overall dimensions of ~180 Å wide, ~110 Å high, and ~120 Å deep. Two MDGA1 monomers flank the NL1 dimer to form a 2-fold symmetric complex. Remarkably, the overall root-mean-square deviation (RMSD)

using small-angle X-ray scattering (SAXS) at a concentration of 30 μM. The scattering data were unambiguously incompatible with a dimeric MDGA1 molecule but were instead accurately ($\chi^2$ = 1.17) modeled as a limited ensemble of monomeric conformers with pronounced flexibility at the $FnIII_7$-$Mam_8$ domain linkage (Figure S2C). In accordance with our SAXS data, we determined using analytical ultracentrifugation (AUC) that human $MDGA1_{ECTO}$ is monomeric at a concentration of 60 μM (Figures S2D and S2E). Finally, to probe whether potential MDGA1 self-association might instead be transient, we performed surface plasmon resonance (SPR) experiments in which wild-type
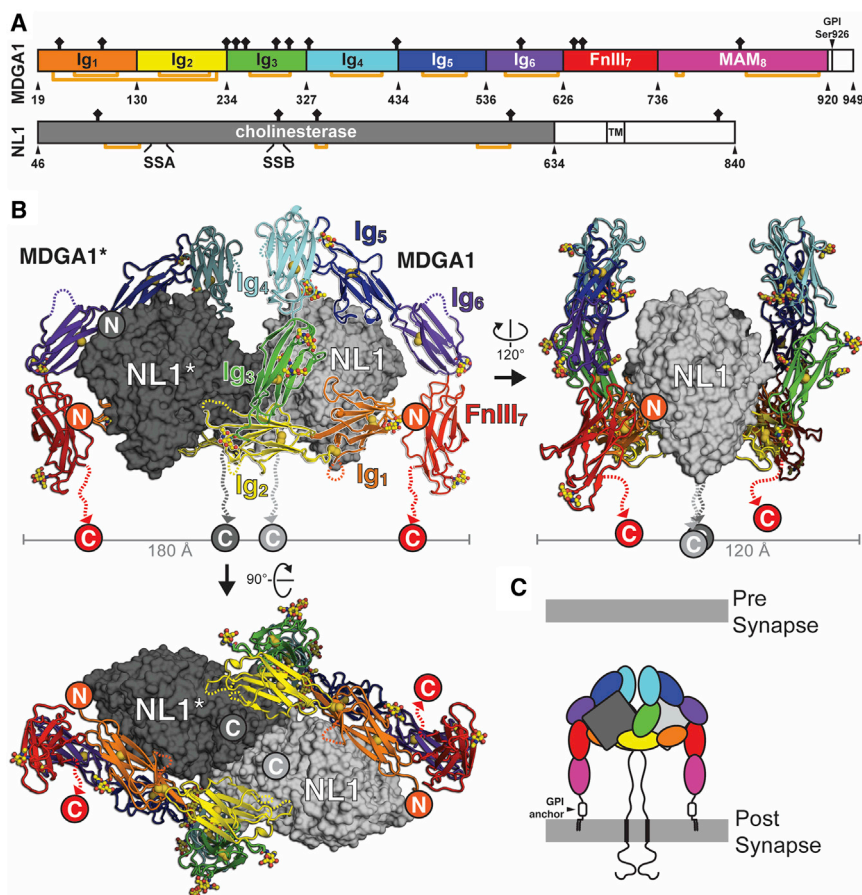
**Figure 2. Crystal Structure of an NL-MDGA Complex**

(A) Schematic representation of the constructs used for co-crystallization of the hNL1(–A–B)$_{ECTO}$-cMDGA1$_{ECTO}$ complex. Orange lines connect cysteine residues engaged in disulfide bonds. SSA and SSB depict the position of spliced sequences A and B on NL1, respectively. The MDGA1 Mam$_8$ domain was included in the crystallization construct but was not observed in the electron density, similar to the free cMDGA1$_{ECTO}$ structure.

(B) Front, 120° rotated side, and 90° rotated bottom views of the hNL1(–A–B)$_{ECTO}$-cMDGA1$_{ECTO}$ complex, shown in surface (NL1) and cartoon (MDGA1) representation. Disulfide bridges are shown as yellow spheres. Glycan moieties visible in the electron density maps are shown in ball and stick representation. The C termini of MDGA1 and NL1 point in the same direction, suggesting a complex formed in *cis*, located on the postsynaptic membrane.

(C) Schematic representation of the postsynaptic NL1-MDGA1 *cis* complex.

See also Figure S3.

between apo and NL1-bound cMDGA1$_{ECTO}$ structures is only 1.5 Å over 647 Cα atoms, underlining the stability and importance of this unusual multi-domain architecture. The NL1 and MDGA1 C termini point in the same direction and thus confirm an interaction in *cis*, situated on the postsynaptic membrane (Figures 2B and 2C). Each MDGA1 molecule spans the NL1 dimer using two large, separate interaction sites located on both NL1 monomers (Sites I and II) (Figure 3A). The Ig$_{1-3}$ domains mediate all MDGA1 contacts, consistent with previous domain-deletion experiments (Pettem et al., 2013). In contrast with the NL-NRX complex (Araç et al., 2007; Chen et al., 2008; Fabrichny et al., 2007), there was no evidence for the presence of coordinated calcium atoms at either Site I or II interfaces.

The numbering scheme employed in all following structural analyses is based on UniProt: P58400 (human β-NRX1), Q0WYX8 (chicken MDGA1), and Q8N2Q7 (human NL1). Annotation of secondary structural elements follows the acetylcholinesterase (AChE) nomenclature (Fabrichny et al., 2007).

The smaller Site I (859 Å$^2$ BSA) is formed between residues from (1) MDGA1$_{Ig1}$ β strands C, F, and G and loop *CE* and (2) NL1 loops Leu289-Gln307, Ile377-Asp385 (part of "loop L1"), Gln392-Tyr398, and Phe496-Pro499 and helices α2(4,5) and α4(6,7) (Figure 3B). His$_{NL1}$291, Tyr$_{NL1}$292, Asp$_{NL1}$384, and Glu$_{NL1}$394 are at the core of Site I. His$_{NL1}$291 and Tyr$_{NL1}$292 make Van der Waals (VdW) contacts and form putative hydrogen

bonds with multiple MDGA1$_{Ig1}$ residues. Asp$_{NL1}$384 and Glu$_{NL1}$394 form putative salt bridges with Arg$_{MDGA1}$105 and Arg$_{MDGA1}$123 (Figure S4A).

The larger Site II (1,000 Å$^2$ BSA) is formed between residues from (2) MDGA1$_{Ig2}$ β strands A, B, D, and E and NL1 α helices α2(7,8) and α3(7,8); (2) MDGA1$_{Ig2}$ loop *AB$_{Ig2}$* and NL1 loops Ala110-Pro132 ("Cys loop") and Asp361-Asp385 ("loop L1"); and (3) peripheral interactions contributed by MDGA1$_{Ig3}$ to NL1 α helix α2(7,8) and loop Val417-Ser424 (Figure 3B). Notably, MDGA1 loops *AB$_{Ig2}$* and *DE$_{Ig2}$* form long protrusions that give Ig$_2$ a concave shape to accommodate the NL1 α helix α2(7,8) (Figure 3B). The Phe$_{NL1}$430-Phe$_{MDGA1}$154 π-π sandwich stacking interaction is central to this interface and is lined by multiple hydrogen-bonding and charged interactions. The tip of MDGA1 loop *AB$_{Ig2}$* extends into a pocket lined predominantly by hydrophobic NL1 residues. Part of loop *AB$_{Ig2}$* (Ile140-Ser146 stretch) could not be resolved in the complex electron density map (Figure S4A).

The NL1 "Cys loop" (part of loop Ala110-Pro132) and "loop L1" (part of loop Asp361-Asp385) occlude the "gorge" that, in AChE, leads to the enzyme active site. Interestingly, these loop structures form an integral part of the NL-MDGA interface. In this sense, MDGA resembles the snake toxin fasciculin (Fas) for binding to AChE (Bourne et al., 1995; Harel et al., 1995). There are, however, no indications that Fas might bind NL and interfere with MDGA binding.

The function of the NL Leu449-Arg450-Glu451 (LRE) adhesion motif, conserved in all NLs and located in the α3(7,8) helix (Figures 7B and S3C), is not clear. The LRE motif was first identified in the extracellular matrix protein laminin β2, where it is involved in binding the Ca$_V$2.2 voltage-gated
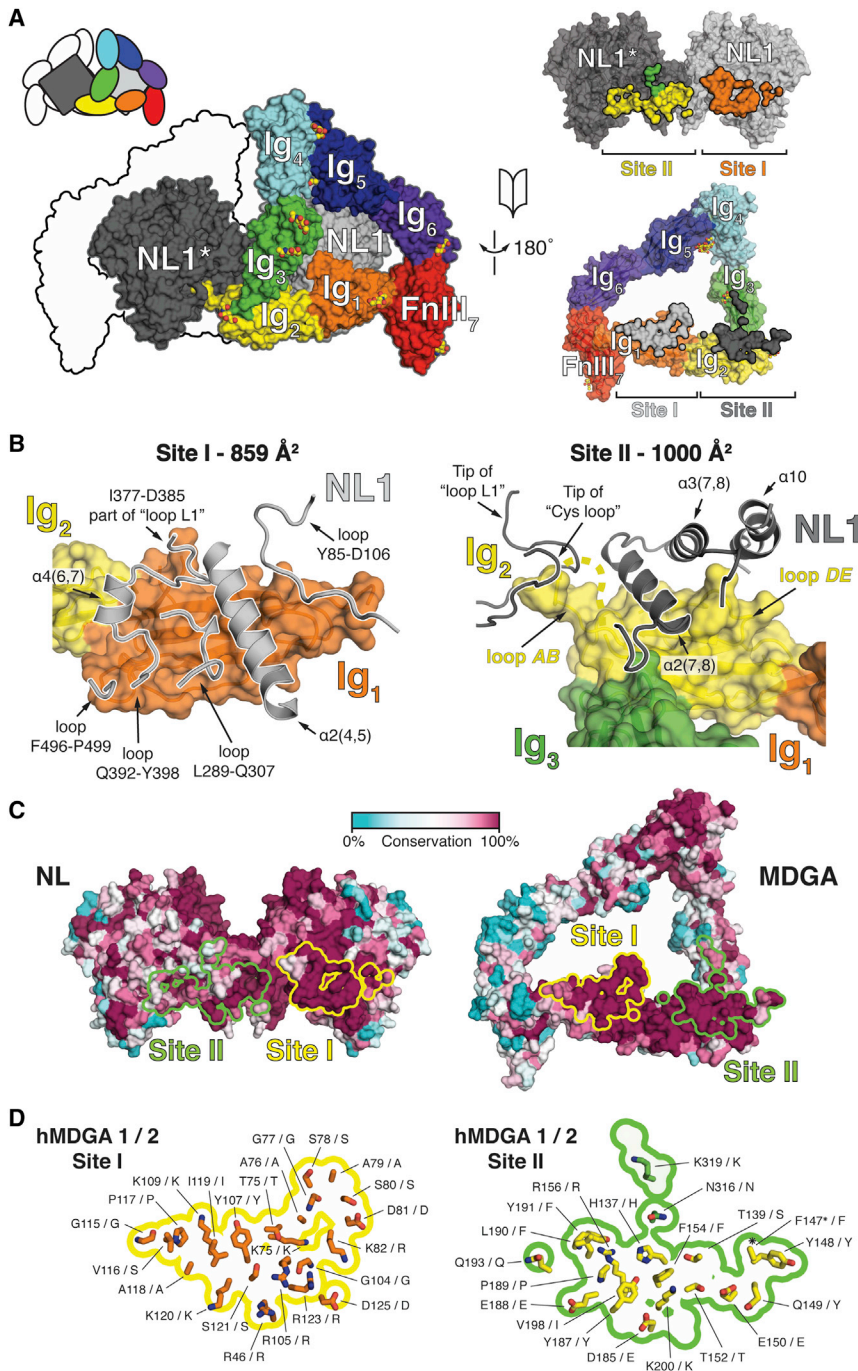
## Figure 3. Details and Conservation of the NL-MDGA Site I and II Interfaces

(A) 180° rotated open book view of the NL1-MDGA1 Site I and Site II interaction interfaces. Site I (859 $Å^2$ buried surface area [BSA]) and Site II (859 $Å^2$ BSA) group interactions contributed by MDGA1 $Ig_1$ and $Ig_2$-$Ig_3$, respectively.

(B) Overview of the NL1 secondary structure elements contacted by $MDGA_{Ig1}$ to form Site I, and $MDGA_{Ig2-3}$ to form Site II.

(C) View of the NL1 and MDGA1 interaction interfaces, color-coded by sequence conservation in vertebrate NL1, NL2, NL3, NL4, and NL5 (1,046 total sequences), and vertebrate MDGA1 and MDGA2 (420 total sequences).

(D) View of the MDGA1 interaction interface. Site I and Site II interfaces are outlined by yellow and green lines, respectively. Per residue position, equivalent residues in human MDGA1 and MDGA2 are annotated to highlight overall sequence conservation of the interaction interfaces. Star symbols (*) indicate residues for which side chain electron density was not clearly discernable.

See also Figure S4.

Sequence conservation analysis indicated that both Site I and Site II interfaces are highly conserved in vertebrate MDGAs and NLs (Figures 3C, 3D, and S4B); this observation strongly points toward a common binding mode between all MDGA and NL family members.
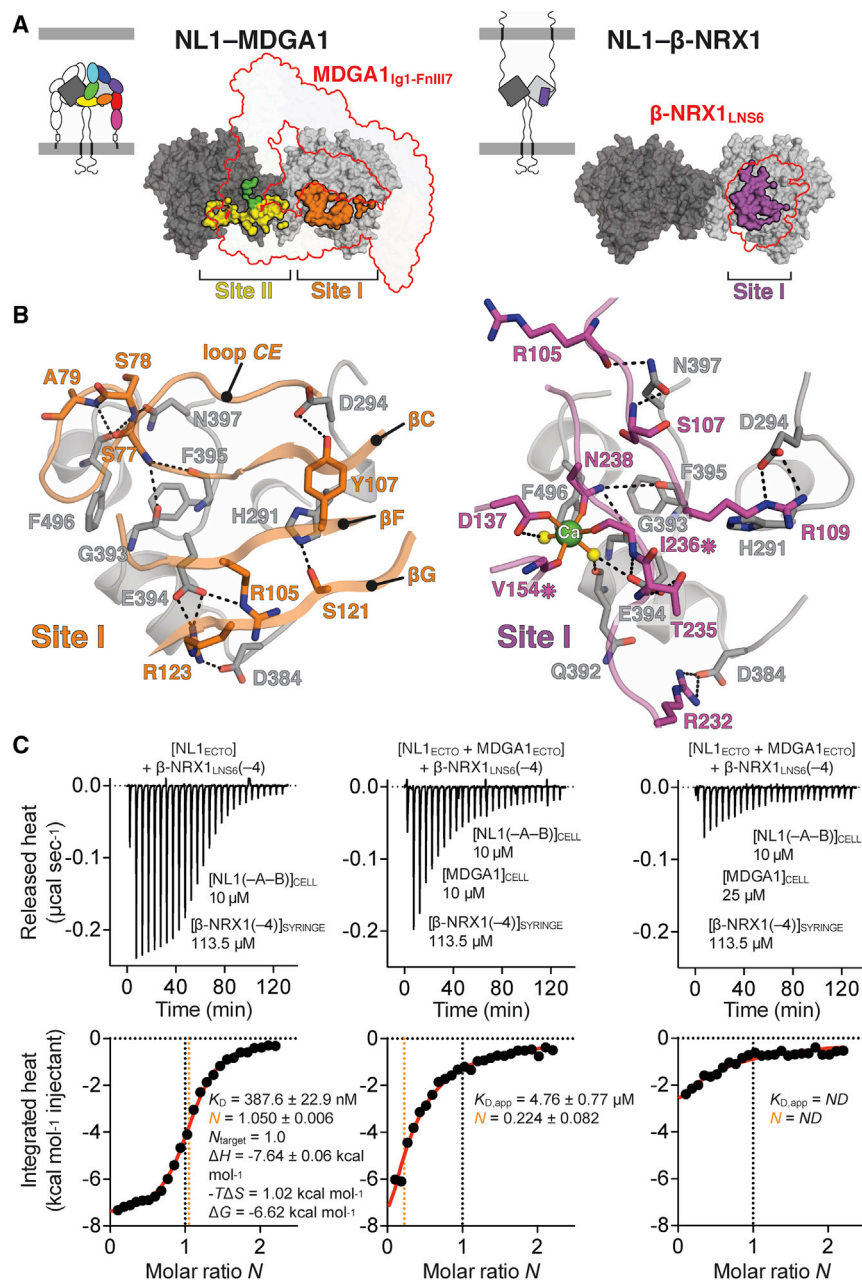
We mapped all predicted N-glycosylation sites for human MDGA1-2 and NL1-5 (NLs lacking splice inserts) on the $cMDGA1_{ECTO}$ and $hNL1_{ECTO}$ structures (Figures S4C and S4D). The MDGA1-specific N-glycan at Asn307, experimentally confirmed by identifying the corresponding N-acetylglucosamine monosaccharide in the $hNL1_{ECTO}$-$cMDGA1_{ECTO}$ electron density map, is the only glycan that is proximal to the binding interface and is situated in $Ig_3$ at the edge of Site II. Analysis of the complex structure, however, indicated that all putative N-linked glycans can project into the solvent, thereby avoiding interference with complex formation. Proteins for subsequent biophysical and cellular experiments were expressed in HEK293T and COS-7 cells, respectively, and were not deglycosylated.

### MDGA and NRX Share Binding Interfaces on NL

We compared our NL1-MDGA1 structure with previously reported NL1-β-NRX1 complexes (Araç et al., 2007; Chen et al., 2008; Fabrichny et al., 2007). Using the highest resolution NL1-β-NRX1 structure available (PDB: 3B3Q; 2.4 Å; Chen et al., 2008), both complexes align with an RMSD of 0.292 Å over

calcium channel. Furthermore, the LRE motif is present in the majority of mammalian AChEs, and besides in NL, it is also observed in the cholinesterase-like adhesion molecules neurotactin and glutactin (Johnson and Moore, 2013). Both Arg450 and Glu451 form an integral part of the NL-MDGA interface and interact with Tyr187 and Leu190, respectively, on MDGA1 loop $DE_{Ig2}$ (Figures 7A and S4A), offering a first functional role for this LRE-tripeptide in NLs.

**Figure 4. MDGA and NRX Compete for Binding to the NL Site I Interface**

(A) Comparison of the NL1-MDGA1 and NL1-β-NRX1 complex binding modes. The NL1-MDGA1 and NL1-β-NRX1 (based on PDB: 3B3Q; Chen et al., 2008) interfaces are oriented similarly, based on structural alignment of one NL1 monomer (0.292 Å RMSD over 453 NL1 Cα positions). The respective molecular footprints of MDGA1 and β-NRX1 are outlined with a red stroke. The NL1-MDGA1 Site I and Site II interfaces, and the NL1-β-NRX1 Site I interface, are shown in surface representation.

(B) Detailed comparison of the core NL1 residues shared between NL1-MDGA1 and NL1-β-NRX1 Site I interfaces. Putative hydrogen bonds and hydrophilic interactions are indicated with black dashed lines. The hexadentate coordination shell of the NL1-β-NRX1 interface calcium (Ca) atom is indicated with solid orange lines.
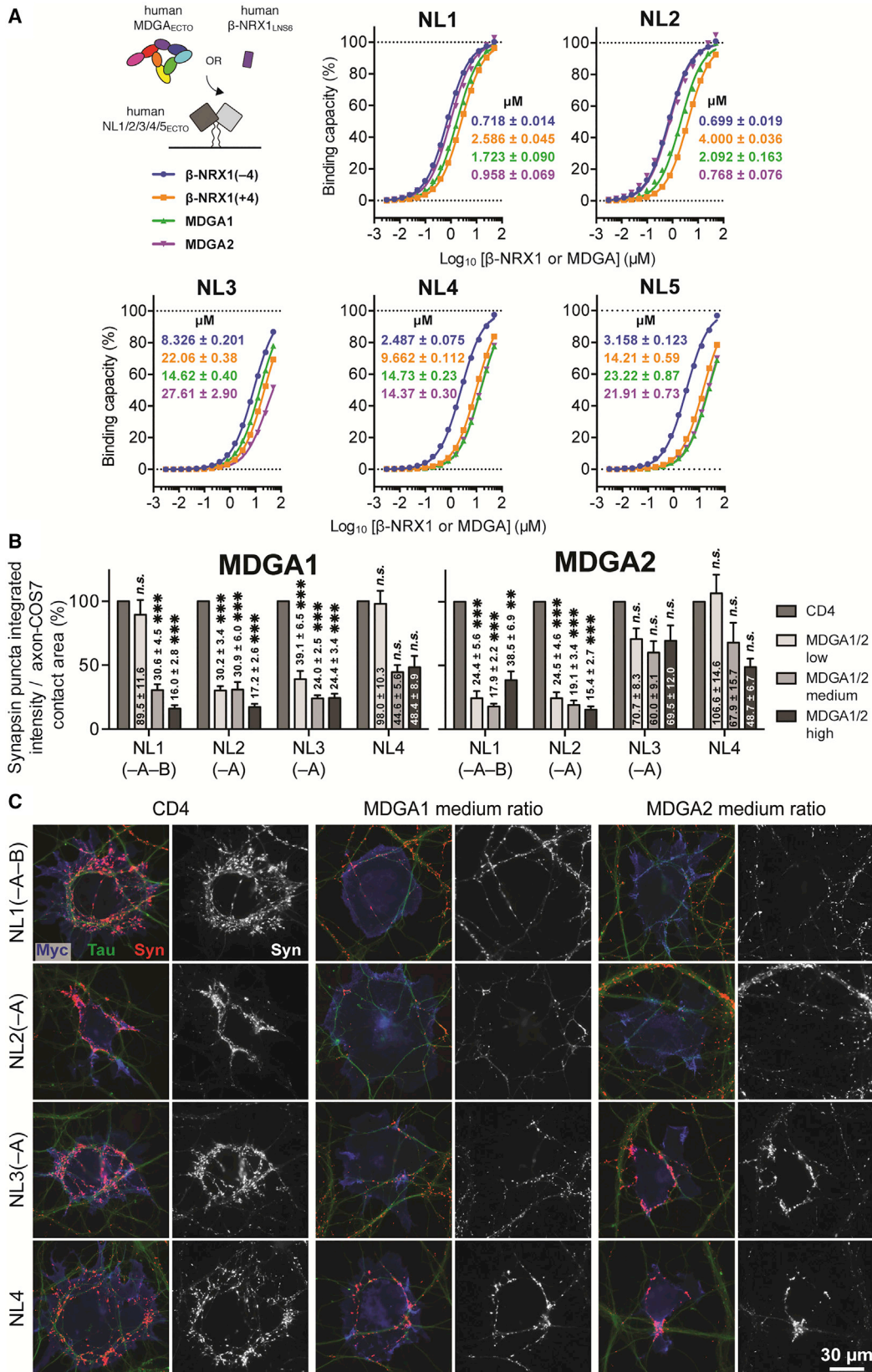
(C) Summary of the calorimetric competition assay binding isotherms, indicating that MDGA1$_{ECTO}$ can compete with β-NRX1$_{LNS6}$(−4) for binding to NL1$_{ECTO}$ in a concentration-dependent fashion. In each case, the experimental geometry is "[cell contents] + syringe contents." For calculation of the stoichiometry, NL1, MDGA1, and β-NRX1(−4) were considered in their monomeric state. Thermodynamic binding parameters are annotated. ND, not determined. An ∼2.5-fold molar excess of MDGA1 was required to fully block binding of β-NRX1$_{LNS6}$(−4) to NL1$_{ECTO}$.

Gly393, Phe395, Phe496, and Asn397 are contacted by MDGA1$_{Ig1}$ loop *CE*, preventing their network of hydrogen-bonded interactions with β-NRX1 residues (Figure 4B).

We set up an isothermal titration calorimetry (ITC) assay to investigate whether MDGA1$_{ECTO}$ competes with β-NRX1$_{LNS6}$ lacking SS4 (β-NRX1$_{LNS6}$(−4)) for binding to NL1$_{ECTO}$. Titration of β-NRX1$_{LNS6}$(−4) into NL1$_{ECTO}$ alone revealed a strong exothermic interaction and a $K_D$ of ∼390 nM. Application of an equimolar amount of MDGA1$_{ECTO}$ to NL1$_{ECTO}$ in the titration cell did not fully block the NL1$_{ECTO}$-β-NRX1$_{LNS6}$(−4) interaction, but decreased its apparent $K_D$ ($K_{D,app}$) ∼12-fold to 4.76 μM. Application of a 2.5-fold molar excess of MDGA1$_{ECTO}$ over NL1$_{ECTO}$ was required to fully block binding of β-NRX1$_{LNS6}$(−4) to NL1$_{ECTO}$ (Figure 4C). These results are consistent with the notion that MDGA is not an ultra-high-affinity decoy receptor, and that by varying the levels of MDGA, the level of NL-NRX complex formation can be tuned.

## MDGA1 and MDGA2 Bind All NL Isoforms

We hypothesized that the interactions between human NLs and MDGAs are not limited to certain pairs of isoforms, given the high level of conservation of the Site I and Site II interface residues

453 NL1 Cα positions. Strikingly, Site I overlaps nearly completely with the NL1-β-NRX1 interface, suggesting that MDGA prevents the NL-NRX interaction via steric hindrance (Figure 4A). Core NL1 residues shared between NL1-MDGA1 and NL1-β-NRX1 interfaces are His291, Asp294, Asp384, Gly393-Asn397, Phe496, and Gly497. Arg$_{MDGA1}$123 mimics Arg$_{β-NRX1}$232 for binding to Asp$_{NL1}$384. Arg$_{MDGA1}$123 and Arg$_{MDGA1}$105 engage Glu$_{NL1}$394 in ionic interactions, whereas in NL1-β-NRX1, the latter residue contacts Thr$_{β-NRX1}$235 and is part of the hexadentate coordination shell of the obligate interface calcium atom. Asp$_{NL1}$294 forms a hydrogen bond with Tyr$_{MDGA1}$107, whereas it forms a bifurcated ionic interaction with Arg$_{β-NRX1}$109 in NL1-β-NRX1. Finally, NL1 residues

**A**

human MDGA_ECTO    human β-NRX1_LNS6

OR

human NL1/2/3/4/5_ECTO

- β-NRX1(−4)
- β-NRX1(+4)
- MDGA1
- MDGA2

**NL1**

Binding capacity (%)

μM
0.718 ± 0.014
2.586 ± 0.045
1.723 ± 0.090
0.958 ± 0.069

$Log_{10}$ [β-NRX1 or MDGA] (μM)

**NL2**

μM
0.699 ± 0.019
4.000 ± 0.036
2.092 ± 0.163
0.768 ± 0.076

**NL3**

Binding capacity (%)

μM
8.326 ± 0.201
22.06 ± 0.38
14.62 ± 0.40
27.61 ± 2.90

**NL4**

μM
2.487 ± 0.075
9.662 ± 0.112
14.73 ± 0.23
14.37 ± 0.30

**NL5**

μM
3.158 ± 0.123
14.21 ± 0.59
23.22 ± 0.87
21.91 ± 0.73

$Log_{10}$ [β-NRX1 or MDGA] (μM)

**B**

Synapsin puncta integrated intensity / axon-COS7 contact area (%)

**MDGA1**

NL1 (−A−B): n.s. 89.5 ± 11.6; *** 30.6 ± 4.5; *** 16.0 ± 2.8
NL2 (−A): *** 30.2 ± 3.4; *** 30.9 ± 6.0; *** 17.2 ± 2.6
NL3 (−A): *** 39.1 ± 6.5; *** 24.0 ± 2.5; *** 24.4 ± 3.4
NL4: n.s. 98.0 ± 10.3; n.s. 44.6 ± 5.6; n.s. 48.4 ± 8.9

**MDGA2**

NL1 (−A−B): *** 24.4 ± 5.6; *** 17.9 ± 2.2; ** 38.5 ± 6.9
NL2 (−A): *** 24.5 ± 4.6; *** 19.1 ± 3.4; *** 15.4 ± 2.7
NL3 (−A): n.s. 70.7 ± 8.3; n.s. 60.0 ± 9.1; n.s. 69.5 ± 12.0
NL4: n.s. 106.6 ± 14.6; n.s. 67.9 ± 15.7; n.s. 48.7 ± 6.7

- CD4
- MDGA1/2 low
- MDGA1/2 medium
- MDGA1/2 high

**C**

CD4 | MDGA1 medium ratio | MDGA2 medium ratio

NL1(−A−B)    Myc  Tau  Syn    Syn

NL2(−A)

NL3(−A)

NL4

30 μm

(legend on next page)

among human NL1–5 and MDGA1-2 (Figures 3C and S4B). To test this, we determined the binding strengths of all pairwise NL-MDGA ectodomain interactions using SPR. We initially focused on the unspliced NL variants for these interaction studies. As a control, we measured the pairwise interactions between NL1–5$_{ECTO}$ and β-NRX1$_{LNS6}$ with and without SS4 (β-NRX1$_{LNS6}$(±4)). The reference interaction of NL1$_{ECTO}$ with β-NRX1$_{LNS6}$(–4) showed an approximately 2-fold higher equilibrium dissociation constant ($K_D$) than the one derived from ITC ($K_D$ of 718 ± 14 nM versus 388 ± 23 nM, respectively; Figures 4C and 5A).

Overall, our measurements revealed $K_D$s for NL-MDGA in the high nanomolar (nM) to low micromolar (μM) range, similar to NL-β-NRX1(±4) (Figure 5A). Accordingly, MDGA does not appear to be an ultra-high-affinity decoy receptor for NL. MDGA1 and MDGA2 interacted most strongly with NL1 and NL2, and MDGA2 binds NL1 and NL2 2-fold stronger than MDGA1 ($K_D$ of ~1 and ~2 μM, respectively). Interaction affinities of MDGA2$_{ECTO}$ and β-NRX1$_{LNS6}$(–4) for NL1–2$_{ECTO}$ are nearly identical. Interestingly, both MDGA1 and MDGA2 interacted ~10- to ~20-fold weaker with NL3, NL4, and NL5 ($K_D$ of ~15–25 μM). Whereas NL3$_{ECTO}$ also binds β-NRX1$_{LNS6}$(–4) with low affinity ($K_D$ of ~8.5 μM), NL4$_{ECTO}$ and NL5$_{ECTO}$ still bind β-NRX1$_{LNS6}$ (–4) relatively strongly ($K_D$ of ~2.5–3 μM), meaning that for NL4 and NL5, a larger discrepancy between binding strengths of β-NRX1(–4) and MDGA1-2 exists (Figure 5A).

Taken together, these experiments show (1) that MDGA1 and MDGA2 have the ability to interact with NLs that localize to excitatory glutamatergic (NL1 and NL3) (Budreck and Scheiffele, 2007; Song et al., 1999), inhibitory GABAergic (NL2 and NL3) (Budreck and Scheiffele, 2007; Graf et al., 2004; Varoqueaux et al., 2004), and inhibitory glycinergic (NL2 and NL4) (Hoon et al., 2011; Varoqueaux et al., 2004) synapses, and (2) that the subtle divergences in NL and MDGA amino acid composition (Figures 3D and S4B) may contribute to subtype preferences. Thus, our results extend the restricted, binary NL-MDGA code that was previously proposed (Connor et al., 2016; Lee et al., 2013; Pettem et al., 2013).

We sought to validate the interaction of MDGA1 and MDGA2 with multiple NLs. To this end, we fused the rat MDGA1 and MDGA2 ectodomains to the Fc region of human IgG. MDGA1- and MDGA2-Fc proteins were then used as bait to identify NLs in postnatal day 21 (P21) rat brain synaptosome extracts, using affinity chromatography coupled with mass spectrometry and bioinformatics analysis (Savas et al., 2014). For extraction, we used the detergent Triton X-100 at 1% w/v concentration. In two independent MDGA1-Fc pull-down experiments, we identified NL3, NL2, and NL1, ranked by spectral count (Figure S5B; Table S2). No peptides for NLs were detected in control experiments using Fc alone or using MDGA lacking Ig$_{1-3}$ (MDGA1ΔIg1–3) (Table S2), demonstrating specificity in the assay. In two independent MDGA2-Fc pull-down experiments, we identified NL2 and, to a lesser extent, NL3 (Figure S5B). In the pull-downs, no NL4 or NL5 was detected; NL4 is of very low abundance (e.g., only ~3% of the total NL in mouse brain; Varoqueaux et al., 2006) and NL5 is restricted to humans. The pull-down results are consistent with our SPR data that indicated a stronger binding of NL3 to MDGA1 than to MDGA2 (Figure 5A).

### MDGA1 and MDGA2 Modulate NL-Induced Recruitment of Hippocampal Synaptic Terminals

To assess whether MDGA1 and MDGA2 are able to broadly modulate NL-NRX-induced synapse formation, we set up a cellular hemi-synapse formation assay in which COS-7 cells co-expressing full-length (FL) N-terminally myc-tagged NL1–4 (myc-NL1–4$_{FL}$) and full-length N-terminally HA-tagged MDGA1-2 (HA-MDGA1-2$_{FL}$) variants were co-cultured with rat hippocampal neurons (Figures 5B, 5C, S6C, and S6D). These neurons express the –SS4 and +SS4 forms of all three α- and β-NRXs (α/β-NRX1-2-3) (Aoto et al., 2013). Accordingly, this assay integrates signals from multiple NRX isoforms, in contrast with our SPR or ITC assays, which only used β-NRX1(±4) as reference interactions (Figures 4C and 5A). To test our hypothesis that by varying the expression levels of MDGA1-2, the extent of NL-NRX complex formation and hence recruitment of synaptic terminals can be influenced, we tested three different plasmid ratios of MDGA1 and MDGA2. For MDGA1, low, medium, and high plasmid ratios designate a 2.2-, 3.5-, and 5.0-fold excess of plasmid DNA over NL, respectively. For MDGA2, these ratios were chosen to be 1.5-fold higher to achieve similar surface protein levels as MDGA1 (Figure S6A). The low ratios used here were similar to the ratios used in our previous co-culture assays of rodent MDGA1-2 with NL1 and NL2 (Connor et al., 2016; Pettem et al., 2013). Similar results were found here for human MDGA1-2 with NL1-2 (see Figures 5B and 8D, low ratio results). However, these earlier studies did not assess the effects of NL alternative splicing, varying ratios of MDGA to NL, or MDGA on NL3-4.

We observed here that MDGA1 and MDGA2 appeared to reduce the ability of all NLs to recruit presynaptic terminals, but with different potency. MDGA1 and MDGA2 both blocked NL1-induced recruitment of synaptic terminals, although a
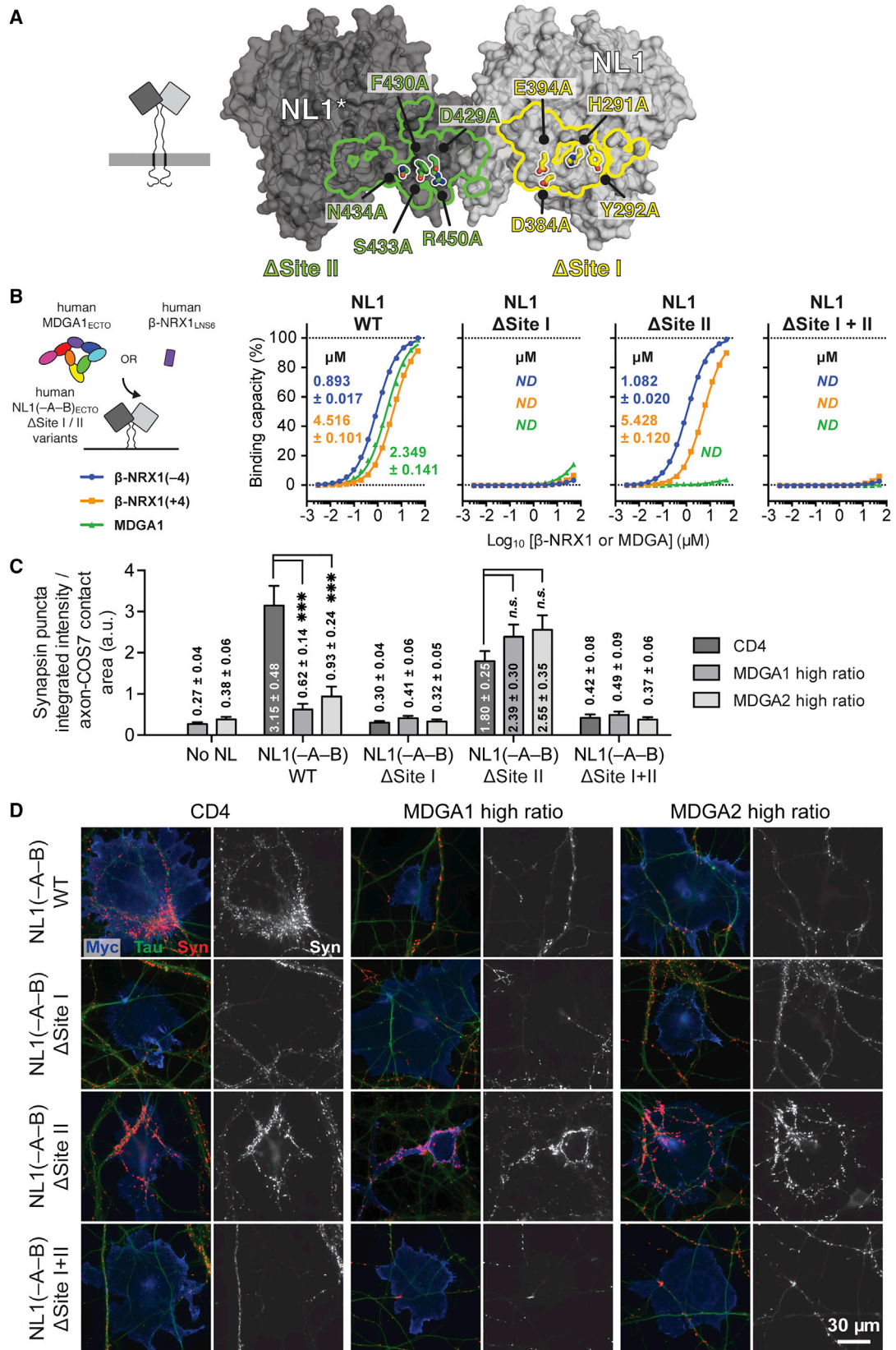
**Figure 5. MDGA1 and MDGA2 Bind All NL Isoforms and Suppress NL-Induced Recruitment of Synaptic Terminals in Co-culture**

(A) Schematic representation of the SPR setup, summary of $K_D$ values, and binding isotherms for the interaction of NL1–5$_{ECTO}$ with MDGA1-2$_{ECTO}$ and β-NRX1$_{LNS6}$(±4).

(B) COS-7 cells expressing myc-NL1–4 were co-transfected with HA-CD4 control, HA-MDGA1, or HA-MDGA2 and co-cultured with hippocampal neurons. The ability of the co-transfected cells to induce synapsin clustering was measured and normalized to the area of tau-positive axon contact. The bar graphs represent the mean of three independent experiments for low, medium, and high plasmid ratios (Figure S6A) of human HA-MDGA1-2:myc-NL1–4 (n > 24 total cells for each condition) with the CD4:myc-NL1–4 co-transfected controls normalized to 100% to show the relative change of synapsin integrated intensity at each ratio. Significance is shown for CD4 control versus MDGAs for each NL (one-way ANOVA with Bonferroni post hoc comparison). Error bars represent the SEM. *p < 0.05, **p < 0.01, ***p < 0.001; n.s., not significant. A detailed statistical quantification can be found in Table S3.

(C) Representative images of co-cultures immunostained for surface myc-NL (blue), surface HA-MDGA or CD4 control (data not shown), synapsin (red), and tau axonal marker (green). The isolated synapsin signal (white) is shown next to each color image. Scale bar, 30 μm.

See also Figures S5 and S6.

**A**

NL1*
NL1

F430A
D429A
E394A
H291A
N434A
S433A
R450A
D384A
Y292A

ΔSite II
ΔSite I

**B**

human MDGA1$_{ECTO}$    human β-NRX1$_{LNS6}$

OR

human NL1(−A−B)$_{ECTO}$ ΔSite I / II variants

- β-NRX1(−4)
- β-NRX1(+4)
- MDGA1

**NL1 WT**

μM
0.893 ± 0.017
4.516 ± 0.101
2.349 ± 0.141

**NL1 ΔSite I**

μM
*ND*
*ND*
*ND*

**NL1 ΔSite II**

μM
1.082 ± 0.020
5.428 ± 0.120
*ND*

**NL1 ΔSite I + II**

μM
*ND*
*ND*
*ND*

Binding capacity (%)

Log$_{10}$ [β-NRX1 or MDGA] (μM)

**C**

Synapsin puncta integrated intensity / axon-COS7 contact area (a.u.)

- CD4
- MDGA1 high ratio
- MDGA2 high ratio

No NL: 0.27 ± 0.04, 0.38 ± 0.06
NL1(−A−B) WT: 3.15 ± 0.48, 0.62 ± 0.14, 0.93 ± 0.24
NL1(−A−B) ΔSite I: 0.30 ± 0.04, 0.41 ± 0.06, 0.32 ± 0.05
NL1(−A−B) ΔSite II: 1.80 ± 0.25, 2.39 ± 0.30, 2.55 ± 0.35
NL1(−A−B) ΔSite I+II: 0.42 ± 0.08, 0.49 ± 0.09, 0.37 ± 0.06

*** ***   *n.s.* *n.s.*

**D**

CD4    MDGA1 high ratio    MDGA2 high ratio

NL1(−A−B) WT
NL1(−A−B) ΔSite I
NL1(−A−B) ΔSite II
NL1(−A−B) ΔSite I+II

Myc  Tau  Syn    Syn

30 μm

*(legend on next page)*

higher ratio was needed to obtain this effect for MDGA1 than for MDGA2 (Figure 5B; Table S3). Both MDGA1 and MDGA2 potently blocked NL2-induced recruitment of synaptic terminals. Thus, there was a weaker effect of MDGA1 on NL1 relative to NL2 activity in this neuron culture-based assay in comparison with similar binding seen with purified proteins in our equilibrium SPR experiments (Figure 5A). Differential effects in the co-culture were not due to any differences in surface levels of MDGAs or NLs (Figure S6B). We observed a stronger differential effect when evaluating NL3-induced synapse formation. Whereas MDGA1 was able to block recruitment of synaptic terminals at all ratios, MDGA2 was not. This is consistent with our SPR analysis, which derived lower responses and corresponding lower interaction affinities for the NL3-MDGA2 interaction (Figures 5A and S5A). Finally, both MDGA1 and MDGA2 were unable to significantly block NL4-induced synapse formation, although there was a trend toward suppression; this agrees with our SPR analysis that indicated that β-NRX1(–4) binds NL4 ∼6-fold stronger than MDGA1-2. We suggest that even higher MDGA:NL plasmid ratios would be needed to fully block NRX binding. However, these conditions were not experimentally accessible in the assay format used, which imposed limits on the total amount of plasmid DNA that can be reliably transfected.

Overall, our results confirm that MDGA1 and MDGA2 can interfere with a broad range of NL-NRX interactions to modulate presynaptic differentiation. The functional outcome will ultimately be influenced by the relative abundances of all molecular players.

### Assessment of Binding of NL1 with Hevin, Thrombospondin-1, and the NMDAR

Given that the interactions of thrombospondin 1 (TSP1) (Xu et al., 2010), hevin (Singh et al., 2016), and the NMDAR (Budreck et al., 2013) with NL1 are all dependent on the coupling of their respective extracellular domains, we hypothesized that MDGA might have the potential to also block binding of these proteins to NL, thereby assigning a more general inhibitory function to MDGA. To test this, we first set out to reproduce the interactions of NL1 with recombinant hevin, TSP1, and NMDAR using SPR. In our setup, secreted human hevin and TSP1 and detergent-solubilized rat NMDAR (GluN1a-GluN2B heterotetramer) (Karakas and Furukawa, 2014) were immobilized on the chip surface (Figure S7A). We found that, in contrast to the reference interaction of NL1(–A–B)$_{ECTO}$ with mouse α-NRX1$_{ECTO}$(–4), all three proteins

failed to interact with NL1(–A–B)$_{ECTO}$ up to a concentration of 25 μM (Figures S7B and S7C).

### Uncoupling of MDGA and NRX Binding to NL

Given that the NL-MDGA crystal structure revealed a composite Site I-II interface, whereas NL-NRX uses only Site I (Figure 4A), we hypothesized that NRX and MDGA binding can be uncoupled, i.e., NL can be rendered insensitive for modulation by MDGA by mutating the Site II interface. We introduced four core interface mutations into the NL1 Site I interface (NL1$^{\Delta Site\ I}$: His291Ala, Tyr292Ala, Asp384Ala, and Glu394Ala) and five into the Site II interface (NL1$^{\Delta Site\ II}$: Asp429Ala, Phe430Ala, Ser433Ala, Asn434Ala, and Arg450Ala) (Figure 6A). We opted to combine multiple mutations of key interface residues instead of using single-position alanine mutants to maximize our chances of obtaining a clear binding differential and cellular phenotype.

Consistent with both NL-MDGA and NL-β-NRX1 complex structures, we found using SPR that the ΔSite II mutant blocked MDGA1 binding but maintained binding of β-NRX1, whereas the ΔSite I and combined ΔSite I+II mutants fully abolished both β-NRX1 and MDGA1 interactions (Figures 6B and S8A).

Using the co-culture assay, we tested the impact of the ΔSite I and ΔSite II mutations on the recruitment of synaptic terminals by full-length NL1. Consistent with our SPR analysis, introduction of the NL1$^{\Delta Site\ I}$ and NL1$^{\Delta Site\ I+II}$ mutations, but not the NL1$^{\Delta Site\ II}$ mutations, prevented NL-NRX-induced synapse formation (Figures 6C and 6D; Table S4). Simultaneously, co-expression at high plasmid ratio of MDGA1 or MDGA2 with NL1 carrying the ΔSite II mutations did not lead to diminished recruitment of synaptic terminals (Figures 6C and 6D; Table S4). We concluded that the NL ΔSite II mutant selectively uncoupled NL-NRX binding and recruitment of synaptic terminals from inhibition by MDGA.

### The ASD-Linked NL3 Mutation Arg451Cys Prevents Suppression of Synapse Formation by MDGA1

The well-characterized NL3 mutation Arg451Cys (R451C) leads to a number of ASD-linked phenotypes in mice (Tabuchi et al., 2007). In this knockin mouse model, R451C acts as a gain-of-function mutation by actually increasing inhibitory synaptic transmission, a result that is seemingly at odds with the severe reduction of NL3 in these mutant mice (Tabuchi et al., 2007). Indeed, complete knockout of NL3 has no such effect (Tabuchi et al., 2007).

**Figure 6. Uncoupling of MDGA and NRX Binding to NL**

(A) Annotation of the NL1 Site I (ΔSite I: H291A, Y292A, D384A, and E394A) and Site II (ΔSite II: D429A, F430A, S433A, N434A, and R450A) mutations.
(B) Schematic representation of the SPR setup, summary of $K_D$ values, and binding isotherms for the interaction of wild-type and mutant human NL1(–A–B)$_{ECTO}$ with MDGA1-2$_{ECTO}$ and β-NRX1$_{LNS6}$(±4).
(C) COS-7 cells expressing myc-NLs were co-transfected with HA-CD4 control, HA-MDGA1, or HA-MDGA2 and co-cultured with hippocampal neurons. The ability of the co-transfected cells to induce synapsin clustering was measured and normalized to the area of tau-positive axon contact. The bar graphs represent the mean of three independent experiments for high plasmid ratios (Figure S6A) of human HA-MDGA1-2:myc-NL1 (n > 22 total cells for each ratio). Significance is shown for CD4 control versus MDGA1-2 for each NL1 variant (one-way ANOVA with Bonferroni post hoc comparison). Error bars represent the SEM. ***p < 0.001; n.s., not significant. Mutation of Site II renders NL1(–A–B) insensitive to suppression of synapse formation by MDGA1 and MDGA2. A detailed statistical quantification can be found in Table S4.
(D) Representative images of co-cultures immunostained for surface myc-NL (blue), surface HA-MDGA or CD4 control (data not shown), synapsin (red), and tau axonal marker (green). The isolated synapsin signal (white) is shown next to each color image. Scale bar, 30 μm.
See also Figure S8.

Our hNL1$_{ECTO}$-cMDGA1$_{ECTO}$ complex crystal structure shows that NL1 Arg450, which is equivalent to NL3 Arg451 and part of the NL1 Leu449-Arg450-Glu451 (LRE) motif (Figures 7B and S3C), is an integral part of the Site II interface (Figure 7A). We introduced the Arg450Cys (R450C) and Arg451Cys (R451C) mutations into NL1(–A–B)$_{ECTO}$ and NL3(–A)$_{ECTO}$, respectively. We observed diminished secretion for the mutants as compared to wild-type proteins (Figure S8B), consistent with reported trafficking defects and protein destabilization (Chih et al., 2004; Comoletti et al., 2004; Tabuchi et al., 2007). Using SPR, we then measured the interaction of β-NRX1(±4) and MDGA1-2 with these mutant proteins and compared them to the wild-type interactions. Our measurements revealed that for both NL1 and NL3, introduction of the R450/451C mutation nearly completely abolished binding of both MDGA1 and MDGA2, while leaving the binding of β-NRX1(±4) unaffected (Figures 7C and S8B). This is consistent with the fact that the R450/451C mutation is situated in the MDGA-specific Site II interface. In this sense, the mutation thus phenocopies our NL1 ΔSite II mutant (Figure 6B).

Using the co-culture assay, we tested the impact of the R451C mutation on the recruitment of synaptic terminals by full-length NL3. Importantly, although impaired relative to wild-type NL3, the R451C mutant can traffic to the surface of transfected COS-7 cells (Figure S8C) and rat hippocampal neurons (Figure S8D; consistent with Chih et al., 2004). Thus, for the co-culture analysis, we again selected COS-7 cells that displayed equal amounts of surface NL to ensure meaningful readout of synapse formation (Figure S8C). Consistent with our SPR analysis, introduction of the R451C mutation had no impact on NL-NRX-induced synapse formation when compared to wild-type NL3 (Figure 7D). Then, co-expression at low plasmid ratio of MDGA1, but not MDGA2, with NL3 wild-type led to diminished recruitment of synaptic terminals. This result closely reproduces our earlier observation (Figure 5B). Introduction of R451C, however, prevented the diminished recruitment of synaptic terminals mediated by MDGA1 (Figures 7D and 7E; Table S5). We concluded that R451C selectively uncoupled NL3-NRX binding and recruitment of synaptic terminals from inhibition by MDGA1.

### Tuning of the NL-MDGA Interaction by NL SSA and SSB

Alternative splicing leads to insertion of SSA and SSB onto the NL cholinesterase scaffold. SSB is restricted to NL1, whereas distinct SSA sequences are present in NL1, NL2, and NL3. In NL1 and NL3, the two possible SSA sequences (A1 and A2) can also occur in tandem (denoted as A1A2) (Figure S3B). Whereas NL1 mRNAs containing and lacking splice insert A are detected at similar levels at hippocampal, cortical, and cerebellar excitatory synapses, mRNA coding for NL1(+B) is more abundant than for NL1(–B) (Chih et al., 2006). Simultaneously, the insertion point for SSB in NL1 is in close proximity to the Site I interface (Koehnke et al., 2010), suggesting that presence of SSB might affect MDGA binding. These observations prompted us to investigate the effect of insertion of SSA and SSB on the NL-MDGA complex formation. First, we mapped SSA, derived from a published NL1(+A1) crystal structure (PDB: 3VKF; Tanaka et al., 2012), onto the NL1-MDGA1 (0.399 Å RMSD over 477 NL1 Cα positions) and NL1-NRX1 (0.375 Å RMSD over 453 NL1 Cα positions) structures (Figure 8B).

Interestingly, although SSA is spatially distant from both Site I and Site II binding interfaces, it is in close proximity to the MDGA Ig$_5$ and Ig$_6$ domains (Figure 8B). As such, SSA might have the potential to either clash with Ig$_5$-Ig$_6$ or, conversely, provide an additional binding site for MDGA. We tested using SPR whether insertion of the distinct SSA sequences into NL1, NL2, or NL3 had an effect on the NL-MDGA or NL-NRX interactions. We were unable to detect a robust or meaningful impact of the SSA sequences on the binding strength of any NL1-3$_{ECTO}$-MDGA1-2$_{ECTO}$ or NL1-3$_{ECTO}$-β-NRX1$_{LNS6}$(±4) pair (Figures S9A, S9B, S10A, and S10B), suggesting that SSA possesses sufficient conformational freedom to not perturb the core NL-MDGA interaction. Accordingly, we suggest that SSA is not involved in modulating the NL-MDGA interaction.

Next, we determined the crystal structure of human NL1 containing SSB (hNL1(+B)) at 2.55 Å (Figure 8A; Table S1). The nine-residue SSB (NRWSNSTKG), inserted between Gly295 and Leu305, was clearly visible in the electron density; the N-linked glycan at Asn300, a modulator of the NL-NRX interaction (Chih et al., 2006; Comoletti et al., 2003), was, however, not fully resolved due to conformational flexibility (Figure 8A). Superposition of NL1(+B) and NL1-MDGA1 (0.308 Å RMSD over 434 NL1 Cα positions) or NL1-NRX1 (0.306 Å RMSD over 428 NL1 Cα positions) structures revealed that SSB is spatially immediately adjacent to both Site I interfaces (Figure 8B). We found, using SPR, that insertion of SSB weakened the NL1-MDGA1-2 interaction ∼7-fold, while reducing the NL1-β-NRX1(±4) interaction less than 2-fold (Figure 8C). We propose that this differential effect is due to the much larger molecular footprint of MDGA and the resulting close proximity of the MDGA Ig$_5$ and Ig$_6$ domains to the N-linked glycan at Asn300, suggesting that SSB reduces the NL-MDGA interaction due to steric hindrance (Figure 8B). Indeed, removal of the N-linked glycan (Asn300Gln mutant) partially recovered the NL1-MDGA1-2 interaction affinity, whereas it had almost no effect on the NL1-β-NRX1(±4) interaction (Figure 8C).

Using the co-culture assay, we tested the effect of the presence of SSB on the ability of MDGA1-2 to block recruitment of synaptic terminals by full-length NL1(–B) and NL1(+B). Co-expression of MDGA1-2 at low, medium, and high plasmid ratios (as previously defined; Figure S6A) led to a decreased recruitment of terminals by both NL1(–B) and NL1(+B) (Figures 8D and 8E; Table S3); however, we found a concentration-dependent decrease for MDGA1. At the medium ratio, MDGA1 significantly blocked recruitment of terminals by NL1(–B), but not NL1(+B), consistent with the difference in binding observed in the SPR assay (Figure 8C). Taken together, our results suggest that, despite the proximity of SSB to the Site I interface, its presence does not eliminate the ability of MDGA to block NL-NRX signaling. Rather, SSB provides a way to fine-tune the NL1-MDGA1-2 interaction at excitatory synapses.

### DISCUSSION

In this work, we present the structure of the near-complete MDGA1 extracellular domain and its complex with NL1, establishing the general recognition paradigm between these synaptic organizing molecules. Simultaneously, our structural analyses
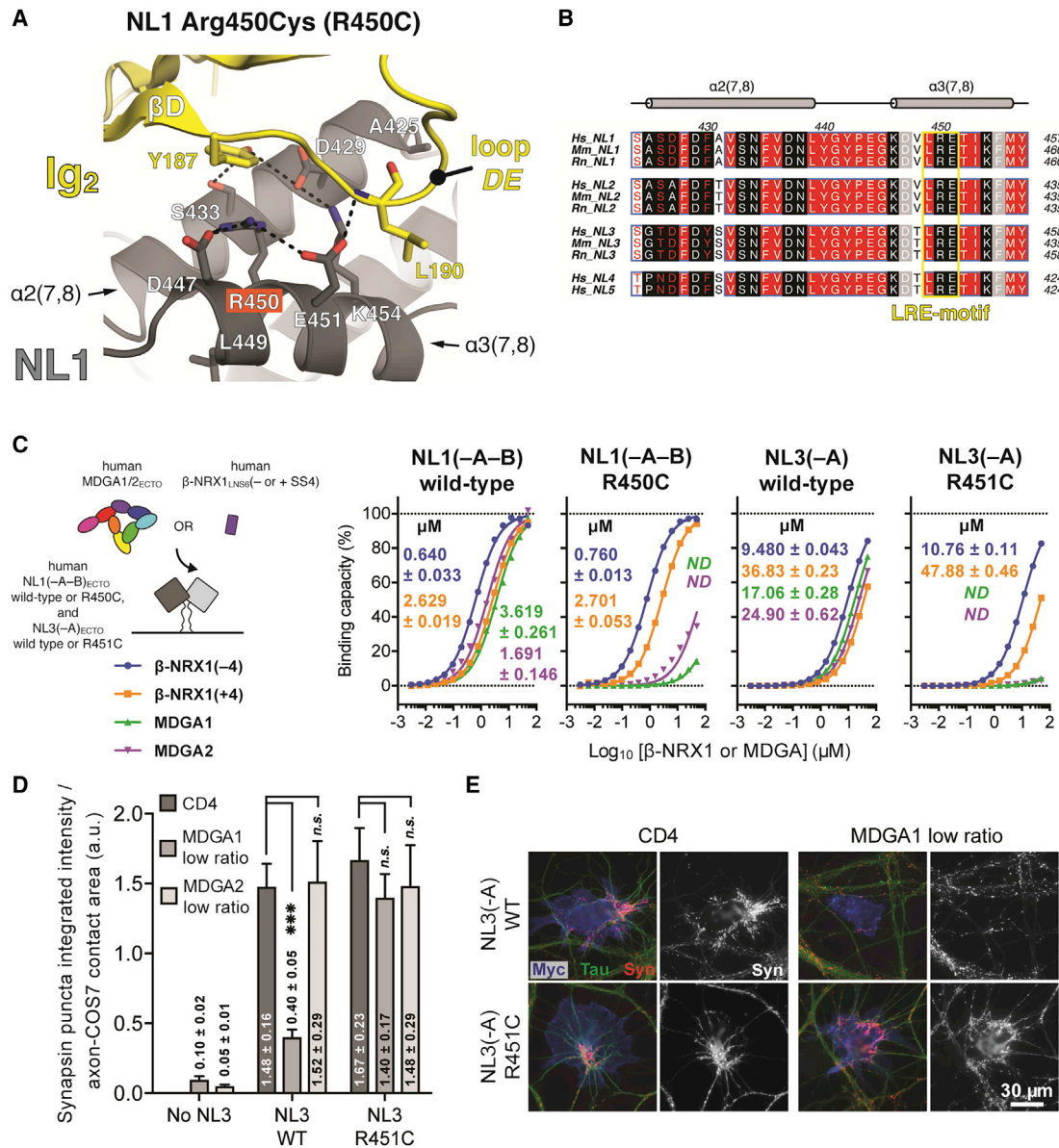
**Figure 7. The ASD-Linked NL3 Mutation Arg451Cys Prevents Suppression of Synapse Formation by MDGA1**

(A) NL1 Arg450, equivalent to NL3 Arg451, is engaged in $\pi$-stacking interactions with $Tyr_{MDGA1}187$ and its side chain is oriented by charged interactions with $Asp_{NL1}447$ and $Glu_{NL1}451$.
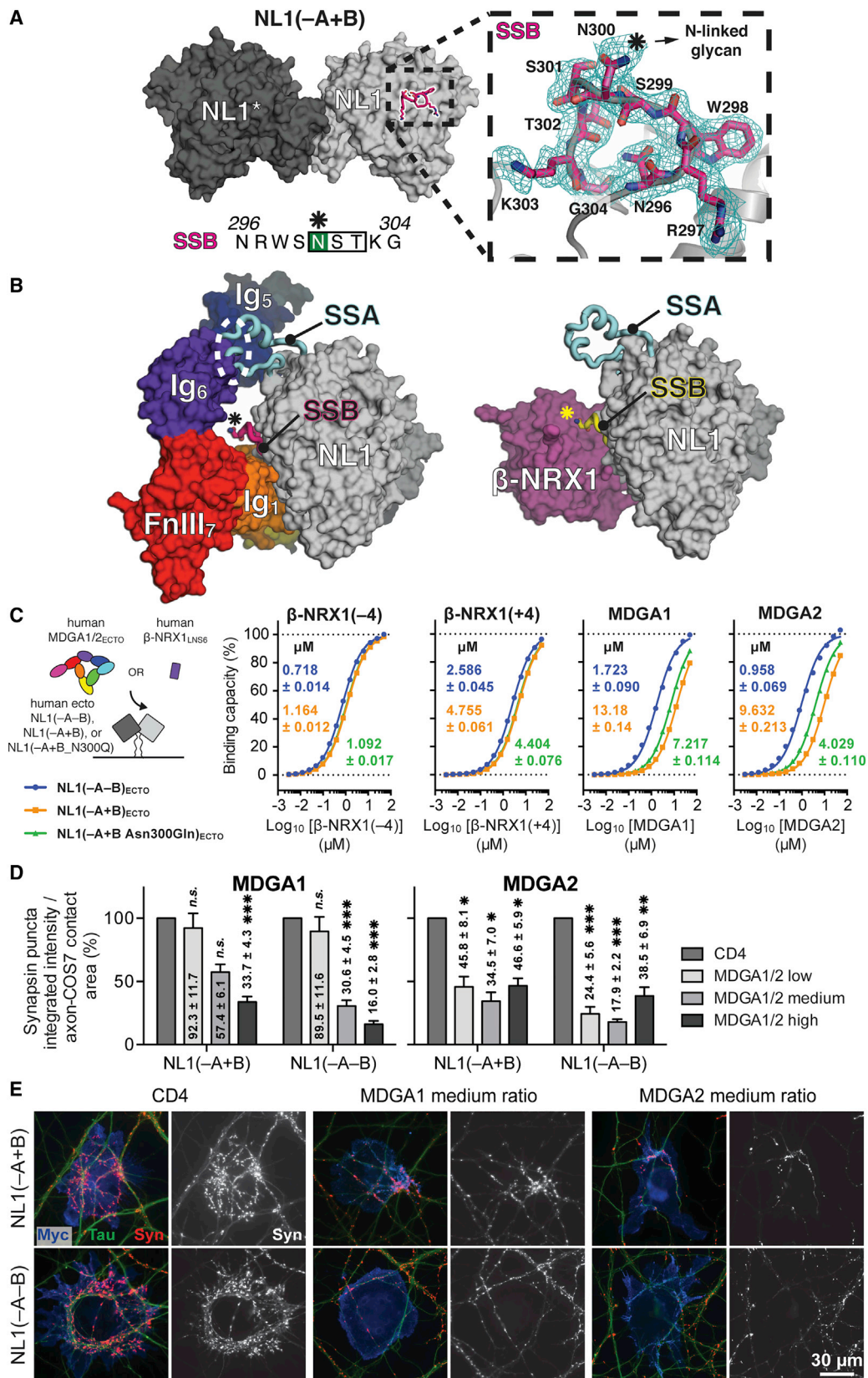
(B) Sequence alignment of human, mouse, and rat NL1–5. Helices $\alpha2(7,8)$ and $\alpha3(7,8)$ of $Hs\_NL1$ are annotated above the alignment. NL residues unique to the "core" and "rim" of the NL-MDGA interface are highlighted in black and gray, respectively. The Leu-Arg-Glu (LRE) motif, conserved in all NLs and located in the $\alpha3(7,8)$ helix, is boxed in yellow. The equivalent NL1 Arg450 and NL3 Arg451 residues are part of the Site II interface and central to the LRE motif. *Hs*; *Homo sapiens*, *Mm*; *Mus musculus*, *Rn*; *Rattus norvegicus*.

(C) Schematic representation of the SPR setup, summary of $K_D$ values, and binding isotherms for the interaction of NL1, NL1 Arg450Cys, NL3, and NL3 Arg451Cys with $MDGA1-2_{ECTO}$ and $\beta-NRX1_{LNS6}(\pm4)$.

(D) COS-7 cells expressing myc-NL3 wild-type or myc-NL3 Arg451Cys were co-transfected with HA-CD4 control, HA-MDGA1, or HA-MDGA2 and co-cultured with hippocampal neurons. The ability of the co-transfected cells to induce synapsin clustering was measured and normalized to the area of tau-positive axon contact. The bar graphs represent the mean of three independent experiments for the low plasmid ratio (Figure S6A) of human HA-MDGA1-2:myc-NL3 (n > 21 total cells for each condition). Significance is shown for CD4 control versus MDGAs (one-way ANOVA with Bonferroni post hoc comparison). Error bars represent the SEM. ***p < 0.001; n.s., not significant. A detailed statistical quantification can be found in Table S5.

(E) Representative images of co-cultures immunostained for surface myc-NL3 (blue), surface HA-MDGA or CD4 control (data not shown), synapsin (red), and tau axonal marker (green). The isolated synapsin signal (white) is shown next to each color image. Scale bar, 30 $\mu$m.

See also Figure S8.

**A** NL1(−A+B)

SSB  
*296*   ✱   *304*  
N R W S [N S T] K G

**B**

**C**

human MDGA1/2ECTO   human β-NRX1LNS6

OR

human ecto NL1(−A−B), NL1(−A+B), or NL1(−A+B_N300Q)

● NL1(−A−B)ECTO  
● NL1(−A+B)ECTO  
● NL1(−A+B Asn300Gln)ECTO

**β-NRX1(−4)**

μM  
0.718 ± 0.014  
1.164 ± 0.012  
1.092 ± 0.017

**β-NRX1(+4)**

μM  
2.586 ± 0.045  
4.755 ± 0.061  
4.404 ± 0.076

**MDGA1**

μM  
1.723 ± 0.090  
13.18 ± 0.14  
7.217 ± 0.114

**MDGA2**

μM  
0.958 ± 0.069  
9.632 ± 0.213  
4.029 ± 0.110

**D**

**MDGA1**

92.3 ± 11.7 *n.s.*  
57.4 ± 6.1 *n.s.*  
33.7 ± 4.3 ***  
89.5 ± 11.6 *n.s.*  
30.6 ± 4.5 ***  
16.0 ± 2.8 ***

**MDGA2**

45.8 ± 8.1 *  
34.5 ± 7.0 *  
46.6 ± 5.9 *  
24.4 ± 5.6 ***  
17.9 ± 2.2 ***  
38.5 ± 6.9 **

■ CD4  
■ MDGA1/2 low  
■ MDGA1/2 medium  
■ MDGA1/2 high

**E**

CD4    MDGA1 medium ratio    MDGA2 medium ratio

Myc  Tau  Syn    Syn

30 μm

*(legend on next page)*

guided the discovery of a broad splicing-modulated interaction network between all MDGA and NL isoforms that is able to block NL-NRX complex formation and modulate NL-induced recruitment of synaptic terminals.

Two large, triangular MDGA1 molecules cradle dimeric NL to shield it from interacting with NRX. We tested whether this arrangement also has the potential to negatively influence the interaction of NL with the astrocyte-secreted proteins TSP1 (Xu et al., 2010) and hevin (Singh et al., 2016) and with the NMDAR (Budreck et al., 2013). However, we failed to reproduce these interactions using SPR. Our results suggest that, at least using isolated recombinantly produced proteins and in an SPR setup with defined components and buffer conditions, these interactions are very weak, require the membrane environment, or are mediated through as-yet-unidentified auxiliary proteins or small-molecule ligands. Future studies will have to identify the exact molecular components required for these interactions.

The structure of the NL1-MDGA1 complex uncovers Site II, a hitherto unrecognized interaction site on NL that is distinct from the canonical NL-NRX Site I interface, highlighting the ability of the NL cholinesterase fold to accommodate a diverse array of ligand interaction modes. Furthermore, the NL ΔSite II mutant is a useful molecular tool to selectively uncouple NL-NRX complex formation from inhibition by MDGA, or from other proteins that would utilize Site II.

MDGA Ig domains 1–3 mediate all contacts with NL (Figure 3A). We speculate that MDGA might have more binding partners besides NL. Indeed, the MDGA1 MAM domain binds a receptor on axons (Fujimura et al., 2006) and enhances cell motility and adhesion to non-MDGA1-expressing cells (Díaz-López et al., 2010). The Ig domains 4–6 are reported to play a role in determining synaptic localization of MDGA1 and MDGA2 (Loh et al., 2016). Adhesive interactions of MDGA with as-yet-unidentified partners may be responsible for the MDGA-dependent aggregation of basal progenitor cells in the subventricular zone (Perez-Garcia and O'Leary, 2016), radial migration of cortical neurons (Takeuchi and O'Leary, 2006), and directed axon outgrowth (Ingold et al., 2015; Joset et al., 2011). The widespread expression of NLs (Varoqueaux et al., 2006) and NRXs (Brown et al., 2011; Górecki et al., 1999) from early postnatal ages also raises the interesting possibility that MDGAs may function to shield NLs at the stage of process outgrowth to prevent premature axon-dendrite adhesion and synaptogenesis.

Given the similar interaction affinities of MDGA1-2 and NRX with NL, the balance between NL-NRX and NL-MDGA complex formation will be determined by their relative abundances and binding availability at each synapse in vivo. The net effect of MDGA on synaptic NL-NRX signaling may be influenced by the presence of other protein partners of MDGA, NRX (LRRTMs, calsyntenin 3, dystroglycan, latrophilin 1, cerebellins, and C1q-like proteins), and NL (hevin, thrombospondin, and NMDARs). The complexity of NL-NRX signaling is compounded even further by the existence of postsynaptic *cis* NL-NRX silencing complexes (Taniguchi et al., 2007) and by the recent report of MDGA-like functions for γ-protocadherins (Molumby et al., 2017).

The capacity of NLs to form heterodimers (Poulopoulos et al., 2012) will differentially affect MDGA and NRX binding since the MDGA interface spans both NL monomers, whereas the NRX interface does not. For example, NL1/3, the most prevalent NL heterodimer located at excitatory synapses (Budreck and Scheiffele, 2007; Poulopoulos et al., 2012), would harbor an asymmetric set of Site I-II interfaces: Site II on one side of the dimer will come from NL3, while Site I will be donated by NL1. At the other side of the dimer, this will be inverted. Since NL3 interacts ~10-fold more weakly with MDGA than NL1(–B) (Figure 5A), a composite interface will likely lead to an intermediate strength binding event. Insertion of SSB into NL1 near Site I, however, brings the affinity of NL1 for MDGA in the range of that of NL3 (Figure 8C).

The direct interaction affinities with NL1 and NL2 do not seem to account for selectivity of MDGAs to suppress excitatory or inhibitory synapses. Consistent with the role of MDGA2 to suppress excitatory synapses in vivo (Connor et al., 2016), MDGA2, but not MDGA1, suppressed the synaptogenic activity of the major NL at excitatory synapses, NL1(+B), in co-culture experiments at low-medium ratios (Figure 8D). Yet MDGA2 showed ~12-fold and MDGA1 ~6-fold greater affinity for the major NL at inhibitory synapses, NL2, than for NL1(+B) (Figures 5A and 8C). Factors other than direct MDGA-NL1-2 binding affinities that may contribute include differential glycosylation, although we could find no indication for such (Figures S4C and S4D); additional interacting proteins; or differential cell-type

**Figure 8. NL1 SSB Differentially Modulates NL1-NRX and NL1-MDGA Complex Formation**

(A) Crystal structure of human NL1(+B). The inset shows 2$m$Fo-$D$Fc electron density contoured at 1.0σ (cyan mesh) for spliced sequence B (SSB). The star symbol indicates the position of the N-linked glycan at Asn300. The glycan tree itself was not visible in the electron density due to structural flexibility.

(B) Structural mapping of spliced sequences A (SSA) and B (SSB) onto NL1. The NL1-MDGA1 and NL1-β-NRX1 interfaces are oriented similarly, based on structural alignment of one NL1 monomer (0.292 Å RMSD over 453 NL1 Cα positions). The position of SSB is derived from the crystal structure of NL1(+B), and the position of SSA is derived from a published crystal structure of rat NL1(+A1) (PDB: 3VKF; Tanaka et al., 2012).

(C) Schematic representation of the SPR setup, summary of $K_D$ values, and binding isotherms for the interaction of human NL1(–A–B)$_{ECTO}$, NL1(–A+B)$_{ECTO}$, and NL1(–A+B_N300Q)$_{ECTO}$ with MDGA1-2$_{ECTO}$ and β-NRX1$_{LNS6}$(±4).

(D) COS-7 cells expressing myc-NLs were co-transfected with HA-CD4 control, HA-MDGA1, or HA-MDGA2 and co-cultured with hippocampal neurons. The ability of the co-transfected cells to induce synapsin clustering was measured and normalized to the area of tau-positive axon contact. The bar graphs represent the mean of three independent experiments for low, medium, and high plasmid ratios (Figure S6A) of human HA-MDGA1-2:myc-NL1(–A ± B) (n > 24 total cells for each ratio) with the CD4:myc-NL1(–A ± B) co-transfected controls normalized to 100% to show the relative change of synapsin integrated intensity at each ratio. Significance is shown for CD4 control versus MDGAs for each NL1 (one-way ANOVA with Bonferroni post hoc comparison). Error bars represent the SEM. *p < 0.05, **p < 0.01, ***p < 0.001; n.s., not significant. A detailed statistical quantification can be found in Table S3.

(E) Representative images of co-cultures immunostained for surface myc-NL (blue), surface HA-MDGA or CD4 control (data not shown), synapsin (red), and tau axonal marker (green). The isolated synapsin signal (white) is shown next to each color image. Scale bar, 30 μm.

See also Figures S9–S11.

expression and subcellular targeting in the brain. As summarized in the introduction, there are conflicting reports on the roles of MDGAs at excitatory versus inhibitory synapses, perhaps related to the use of different model systems, reinforcing the need to consider the native abundance of each molecular player. The newly discovered interaction of MDGAs with NL3 and NL4, particularly the strong association of MDGA1 with NL3 in the pull-down assay and functional modulation of NL3 by MDGA1 in co-culture, may help in better understanding the roles of MDGAs in specific circuits in vivo.

In the rat and mouse brain, MDGA1 and MDGA2 are widely expressed by neuronal populations in both the central and peripheral nervous systems. These include neurons of the basilar pons, inferior olivary nucleus, cerebellum, cerebral cortex, olfactory bulb, spinal cord, dorsal root and trigeminal ganglia, and hippocampus (Connor et al., 2016; Lee et al., 2013; Litwack et al., 2004; Takeuchi et al., 2007). There are regional differences: for example, MDGA1 is more abundant in superficial cortical layers and MDGA2 in deep layers. NL and NRX are also very widely expressed in the mouse brain, such that most neurons likely express NL1–4 and NRX1–3 at varying levels (Hoon et al., 2011; Ullrich et al., 1995; Varoqueaux et al., 2006). We propose that the structural mechanism we described here will be representative for the full range of CNS synapses at which NL, NRX, and MDGA family members are present. Through NL2 and NL4, the range of synapses modulated by MDGA is likely to include glycinergic synapses, not just GABAergic and glutamatergic synapses as shown previously. The differential affinities of specific MDGA and NL isoforms as well as isoform selective interactions of NL with NRX, interactions with other partners regulating bioavailability, and cell-type expression patterns of all molecular players will serve to fine-tune MDGA modulation of synapse development and function.

An important finding of this study is the discovery that both MDGAs interact with and regulate NL3 and NL4. This is of particular interest since rare mutations in NLs, particularly NL3 and NL4, have been associated with ASD and schizophrenia in human genetic studies (Südhof, 2008; Simons Foundation Autism Research Initiative database, https://gene.sfari.org). Interestingly, two mutations in the MDGA interaction-selective Site II of NL3 have been reported in patients with ASD: Arg451Cys (R451C; corresponding to NL1 residue Arg450 and part of the Leu449-Arg450-Glu451 LRE motif) and Gly426Ser (G426S; corresponding to NL1 residue Ala425) (Jamain et al., 2003; Xu et al., 2014) (Figures 7A and 7B). This raises the possibility that selective modulation of MDGA binding to NLs in patients carrying mutations in Site II could contribute to the development of ASD. R451C was characterized as an NL3 gain-of-function mutation in mice, leading to both increased inhibitory synaptic transmission in the somatosensory cortex (Tabuchi et al., 2007) and increased excitatory synaptic transmission in the hippocampus (Etherton et al., 2011), despite resulting in trafficking defects and protein destabilization (Chih et al., 2004; Comoletti et al., 2004). Nonetheless, we observed surface expression of the mutant in both transfected COS-7 cells (Figure S8C) and rat hippocampal neurons (Figure S8D). The latter observation agrees with a report showing cell-surface expression of NL3 R451C in a subset of transfected hippocampal neurons with high expression level (Chih et al., 2004). This also led to an increase in the number of contacting presynaptic terminals, suggesting that the NL3 R451C that trafficked to the surface is functional (Chih et al., 2004). Importantly, we found that, similarly to the NL ΔSite II mutant, the NL3 R451C mutation selectively uncoupled NL3-NRX binding and recruitment of synaptic terminals from inhibition by MDGA1 (Figure 7D), suggesting that the R451C gain-of-function phenotype is achieved by preventing the inhibition of NL3 by MDGA1, thereby leading to disruption of the overall balance of excitatory/inhibitory (E/I) synaptic transmission.

An E/I imbalance surpassing the capacity of neuronal populations and circuits to regulate synaptic homeostasis is a proposed hallmark of ASD (Nelson and Valakh, 2015; Rubenstein and Merzenich, 2003). Disruptions in the regulatory NL-MDGA network we report here contribute to ASD based on human genetics (Bucan et al., 2009; Kähler et al., 2008; Li et al., 2011; Südhof, 2008) and can generate such an E/I imbalance in animal models (e.g., Connor et al., 2016; Tabuchi et al., 2007). Our findings considerably broadened this interaction network beyond that previously envisioned. Moreover, our structural studies constitute an essential guide toward the generation of directed therapies targeting these gene products to restore E/I balance.

## STAR★METHODS

Detailed methods are provided in the online version of this paper and include the following:

- KEY RESOURCES TABLE
- CONTACT FOR REAGENT AND RESOURCE SHARING
- METHOD DETAILS
  - Expression and purification of recombinant proteins
  - Expression and purification of recombinant NMDA receptor
  - Gene splicing and site-directed mutagenesis
  - Protein crystallization
  - Crystallographic data collection and structure determination
  - Crystallographic refinement and model analysis
  - Sequence alignments and conservation analysis
  - Small-angle X-ray scattering (SAXS)
  - Surface plasmon resonance (SPR) with soluble proteins
  - Surface plasmon resonance (SPR) with the NMDA receptor
  - Isothermal titration calorimetry (ITC)
  - Analytical ultracentrifugation (AUC)
  - Co-culture and immunocytochemistry
  - Image acquisition and analysis
  - Surface expression of the NL3(–A) Arg451Cys mutant
  - Pulldown and mass spectrometry
- DATA AND SOFTWARE AVAILABILITY

### SUPPLEMENTAL INFORMATION

Supplemental Information includes eleven figures and five tables and can be found with this article online at http://dx.doi.org/10.1016/j.neuron.2017.07.040.

**REFERENCES**

Adams, P.D., Afonine, P.V., Bunkóczi, G., Chen, V.B., Davis, I.W., Echols, N., Headd, J.J., Hung, L.W., Kapral, G.J., Grosse-Kunstleve, R.W., et al. (2010). PHENIX: a comprehensive Python-based system for macromolecular structure solution. Acta Crystallogr. D Biol. Crystallogr. 66, 213–221.

Altschul, S.F., Gish, W., Miller, W., Myers, E.W., and Lipman, D.J. (1990). Basic local alignment search tool. J. Mol. Biol. 215, 403–410.

Aoto, J., Martinelli, D.C., Malenka, R.C., Tabuchi, K., and Südhof, T.C. (2013). Presynaptic neurexin-3 alternative splicing trans-synaptically controls postsynaptic AMPA receptor trafficking. Cell 154, 75–88.

Araç, D., Boucard, A.A., Ozkan, E., Strop, P., Newell, E., Südhof, T.C., and Brunger, A.T. (2007). Structures of neuroligin-1 and the neuroligin-1/neurexin-1 beta complex reveal specific protein-protein and protein-Ca2+ interactions. Neuron 56, 992–1003.

Aricescu, A.R., Hon, W.C., Siebold, C., Lu, W., van der Merwe, P.A., and Jones, E.Y. (2006a). Molecular analysis of receptor protein tyrosine phosphatase mu-mediated cell adhesion. EMBO J. 25, 701–712.

Aricescu, A.R., Lu, W., and Jones, E.Y. (2006b). A time- and cost-efficient system for high-level protein production in mammalian cells. Acta Crystallogr. D Biol. Crystallogr. 62, 1243–1250.

Ashkenazy, H., Erez, E., Martz, E., Pupko, T., and Ben-Tal, N. (2010). ConSurf 2010: calculating evolutionary conservation in sequence and structure of proteins and nucleic acids. Nucleic Acids Res. 38, W529-33.

Bemben, M.A., Shipman, S.L., Nicoll, R.A., and Roche, K.W. (2015). The cellular and molecular landscape of neuroligins. Trends Neurosci. 38, 496–505.

Biasini, M., Bienert, S., Waterhouse, A., Arnold, K., Studer, G., Schmidt, T., Kiefer, F., Gallo Cassarino, T., Bertoni, M., Bordoli, L., and Schwede, T. (2014). SWISS-MODEL: modelling protein tertiary and quaternary structure using evolutionary information. Nucleic Acids Res. 42, W252-8.

Bond, C.S., and Schüttelkopf, A.W. (2009). ALINE: a WYSIWYG protein-sequence alignment editor for publication-quality alignments. Acta Crystallogr. D Biol. Crystallogr. 65, 510–512.

Boucard, A.A., Chubykin, A.A., Comoletti, D., Taylor, P., and Südhof, T.C. (2005). A splice code for trans-synaptic cell adhesion mediated by binding of neuroligin 1 to alpha- and beta-neurexins. Neuron 48, 229–236.

Bourne, Y., Taylor, P., and Marchot, P. (1995). Acetylcholinesterase inhibition by fasciculin: crystal structure of the complex. Cell 83, 503–512.

Brautigam, C.A. (2015). Calculations and publication-quality illustrations for analytical ultracentrifugation data. Methods Enzymol. 562, 109–133.

Brown, P.H., and Schuck, P. (2006). Macromolecular size-and-shape distributions by sedimentation velocity analytical ultracentrifugation. Biophys. J. 90, 4651–4661.

Brown, S.M., Clapcote, S.J., Millar, J.K., Torrance, H.S., Anderson, S.M., Walker, R., Rampino, A., Roder, J.C., Thomson, P.A., Porteous, D.J., and Evans, K.L. (2011). Synaptic modulators Nrxn1 and Nrxn3 are disregulated in a Disc1 mouse model of schizophrenia. Mol. Psychiatry 16, 585–587.

Bucan, M., Abrahams, B.S., Wang, K., Glessner, J.T., Herman, E.I., Sonnenblick, L.I., Alvarez Retuerto, A.I., Imielinski, M., Hadley, D., Bradfield, J.P., et al. (2009). Genome-wide analyses of exonic copy number variants in a family-based study point to novel autism susceptibility genes. PLoS Genet. 5, e1000536.

Budreck, E.C., and Scheiffele, P. (2007). Neuroligin-3 is a neuronal adhesion protein at GABAergic and glutamatergic synapses. Eur. J. Neurosci. 26, 1738–1748.

Budreck, E.C., Kwon, O.B., Jung, J.H., Baudouin, S., Thommen, A., Kim, H.S., Fukazawa, Y., Harada, H., Tabuchi, K., Shigemoto, R., et al. (2013). Neuroligin-1 controls synaptic abundance of NMDA-type glutamate receptors through extracellular coupling. Proc. Natl. Acad. Sci. USA 110, 725–730.

Chen, X., Liu, H., Shim, A.H., Focia, P.J., and He, X. (2008). Structural basis for synaptic adhesion mediated by neuroligin-neurexin interactions. Nat. Struct. Mol. Biol. 15, 50–56.

Chen, V.B., Arendall, W.B., 3rd, Headd, J.J., Keedy, D.A., Immormino, R.M., Kapral, G.J., Murray, L.W., Richardson, J.S., and Richardson, D.C. (2010). MolProbity: all-atom structure validation for macromolecular crystallography. Acta Crystallogr. D Biol. Crystallogr. 66, 12–21.

Chih, B., Afridi, S.K., Clark, L., and Scheiffele, P. (2004). Disorder-associated mutations lead to functional inactivation of neuroligins. Hum. Mol. Genet. 13, 1471–1477.

Chih, B., Gollan, L., and Scheiffele, P. (2006). Alternative splicing controls selective trans-synaptic interactions of the neuroligin-neurexin complex. Neuron 51, 171–178.

Comoletti, D., Flynn, R., Jennings, L.L., Chubykin, A., Matsumura, T., Hasegawa, H., Südhof, T.C., and Taylor, P. (2003). Characterization of the interaction of a recombinant soluble neuroligin-1 with neurexin-1beta. J. Biol. Chem. 278, 50497–50505.

Comoletti, D., De Jaco, A., Jennings, L.L., Flynn, R.E., Gaietta, G., Tsigelny, I., Ellisman, M.H., and Taylor, P. (2004). The Arg451Cys-neuroligin-3 mutation associated with autism reveals a defect in protein processing. J. Neurosci. 24, 4889–4893.

Connor, S.A., Ammendrup-Johnsen, I., Chan, A.W., Kishimoto, Y., Murayama, C., Kurihara, N., Tada, A., Ge, Y., Lu, H., Yan, R., et al. (2016). Altered cortical dynamics and cognitive function upon haploinsufficiency of the autism-linked excitatory synaptic suppressor MDGA2. Neuron 91, 1052–1068.

de Wit, J., and Ghosh, A. (2016). Specification of synaptic connectivity by cell surface interactions. Nat. Rev. Neurosci. 17, 22–35.

Díaz-López, A., Iniesta, P., Morán, A., Ortega, P., Fernández-Marcelo, T., Sánchez-Pernaute, A., Torres, A.J., Benito, M., and De Juan, C. (2010). Expression of human MDGA1 increases cell motility and cell-cell adhesion and reduces adhesion to extracellular matrix proteins in MDCK cells. Cancer Microenviron. 4, 23–32.

Edgar, R.C. (2004). MUSCLE: multiple sequence alignment with high accuracy and high throughput. Nucleic Acids Res. 32, 1792–1797.

Elegheert, J., Kakegawa, W., Clay, J.E., Shanks, N.F., Behiels, E., Matsuda, K., Kohda, K., Miura, E., Rossmann, M., Mitakidis, N., et al. (2016). Structural basis for integration of GluD receptors within synaptic organizer complexes. Science 353, 295–299.

Emsley, P., Lohkamp, B., Scott, W.G., and Cowtan, K. (2010). Features and development of Coot. Acta Crystallogr. D Biol. Crystallogr. 66, 486–501.

Etherton, M., Földy, C., Sharma, M., Tabuchi, K., Liu, X., Shamloo, M., Malenka, R.C., and Südhof, T.C. (2011). Autism-linked neuroligin-3 R451C mutation differentially alters hippocampal and cortical synaptic function. Proc. Natl. Acad. Sci. USA 108, 13764–13769.

Evans, P. (2006). Scaling and assessment of data quality. Acta Crystallogr. D Biol. Crystallogr. 62, 72–82.

Evans, P.R. (2011). An introduction to data reduction: space-group determination, scaling and intensity statistics. Acta Crystallogr. D Biol. Crystallogr. 67, 282–292.

Fabrichny, I.P., Leone, P., Sulzenbacher, G., Comoletti, D., Miller, M.T., Taylor, P., Bourne, Y., and Marchot, P. (2007). Structural analysis of the synaptic protein neuroligin and its beta-neurexin complex: determinants for folding and cell adhesion. Neuron 56, 979–991.

Fujimura, Y., Iwashita, M., Matsuzaki, F., and Yamamoto, T. (2006). MDGA1, an IgSF molecule containing a MAM domain, heterophilically associates with axon- and muscle-associated binding partners through distinct structural domains. Brain Res. 1101, 12–19.

Górecki, D.C., Szklarczyk, A., Lukasiuk, K., Kaczmarek, L., and Simons, J.P. (1999). Differential seizure-induced and developmental changes of neurexin expression. Mol. Cell. Neurosci. 13, 218–227.

Graf, E.R., Zhang, X., Jin, S.X., Linhoff, M.W., and Craig, A.M. (2004). Neurexins induce differentiation of GABA and glutamate postsynaptic specializations via neuroligins. Cell 119, 1013–1026.

Guttman, M., Weinkam, P., Sali, A., and Lee, K.K. (2013). All-atom ensemble modeling to analyze small-angle x-ray scattering of glycosylated proteins. Structure 21, 321–331.

Hammel, M. (2012). Validation of macromolecular flexibility in solution by small-angle X-ray scattering (SAXS). Eur. Biophys. J. 41, 789–799.

Harel, M., Kleywegt, G.J., Ravelli, R.B., Silman, I., and Sussman, J.L. (1995). Crystal structure of an acetylcholinesterase-fasciculin complex: interaction of a three-fingered toxin from snake venom with its target. Structure 3, 1355–1366.

Heckman, K.L., and Pease, L.R. (2007). Gene splicing and mutagenesis by PCR-driven overlap extension. Nat. Protoc. 2, 924–932.

Hoon, M., Soykan, T., Falkenburger, B., Hammer, M., Patrizi, A., Schmidt, K.F., Sassoè-Pognetto, M., Löwel, S., Moser, T., Taschenberger, H., et al. (2011). Neuroligin-4 is localized to glycinergic postsynapses and regulates inhibition in the retina. Proc. Natl. Acad. Sci. USA 108, 3053–3058.

Howarth, M., Liu, W., Puthenveetil, S., Zheng, Y., Marshall, L.F., Schmidt, M.M., Wittrup, K.D., Bawendi, M.G., and Ting, A.Y. (2008). Monovalent, reduced-size quantum dots for imaging receptors on living cells. Nat. Methods 5, 397–399.

Ingold, E., Vom Berg-Maurer, C.M., Burckhardt, C.J., Lehnherr, A., Rieder, P., Keller, P.J., Stelzer, E.H., Greber, U.F., Neuhauss, S.C., and Gesemann, M. (2015). Proper migration and axon outgrowth of zebrafish cranial motoneuron subpopulations require the cell adhesion molecule MDGA2A. Biol. Open 4, 146–154.

Jamain, S., Quach, H., Betancur, C., Råstam, M., Colineaux, C., Gillberg, I.C., Soderstrom, H., Giros, B., Leboyer, M., Gillberg, C., and Bourgeron, T.; Paris Autism Research International Sibpair Study (2003). Mutations of the X-linked genes encoding neuroligins NLGN3 and NLGN4 are associated with autism. Nat. Genet. 34, 27–29.

Johnson, G., and Moore, S.W. (2013). The Leu-Arg-Glu (LRE) adhesion motif in proteins of the neuromuscular junction with special reference to proteins of the carboxylesterase/cholinesterase family. Comp. Biochem. Physiol. Part D Genomics Proteomics 8, 231–243.

Joset, P., Wacker, A., Babey, R., Ingold, E.A., Andermatt, I., Stoeckli, E.T., and Gesemann, M. (2011). Rostral growth of commissural axons requires the cell adhesion molecule MDGA2. Neural Dev. 6, 22.

Kabsch, W. (2010). Xds. Acta Crystallogr. D Biol. Crystallogr. 66, 125–132.

Kaech, S., and Banker, G. (2006). Culturing hippocampal neurons. Nat. Protoc. 1, 2406–2415.

Kähler, A.K., Djurovic, S., Kulle, B., Jönsson, E.G., Agartz, I., Hall, H., Opjordsmoen, S., Jakobsen, K.D., Hansen, T., Melle, I., et al. (2008). Association analysis of schizophrenia on 18 genes involved in neuronal migration: MDGA1 as a new susceptibility gene. Am. J. Med. Genet. B. Neuropsychiatr. Genet. 147B, 1089–1100.

Karakas, E., and Furukawa, H. (2014). Crystal structure of a heterotetrameric NMDA receptor ion channel. Science 344, 992–997.

Koehnke, J., Katsamba, P.S., Ahlsen, G., Bahna, F., Vendome, J., Honig, B., Shapiro, L., and Jin, X. (2010). Splice form dependence of beta-neurexin/neuroligin binding interactions. Neuron 67, 61–74.

Krissinel, E., and Henrick, K. (2007). Inference of macromolecular assemblies from crystalline state. J. Mol. Biol. 372, 774–797.

Kvansakul, M., Adams, J.C., and Hohenester, E. (2004). Structure of a thrombospondin C-terminal fragment reveals a novel calcium core in the type 3 repeats. EMBO J. 23, 1223–1233.

Lee, K., Kim, Y., Lee, S.J., Qiang, Y., Lee, D., Lee, H.W., Kim, H., Je, H.S., Südhof, T.C., and Ko, J. (2013). MDGAs interact selectively with neuroligin-2 but not other neuroligins to regulate inhibitory synapse development. Proc. Natl. Acad. Sci. USA 110, 336–341.

Li, J., Liu, J., Feng, G., Li, T., Zhao, Q., Li, Y., Hu, Z., Zheng, L., Zeng, Z., He, L., et al. (2011). The MDGA1 gene confers risk to schizophrenia and bipolar disorder. Schizophr. Res. 125, 194–200.

Litwack, E.D., Babey, R., Buser, R., Gesemann, M., and O'Leary, D.D. (2004). Identification and characterization of two novel brain-derived immunoglobulin superfamily members with a unique structural organization. Mol. Cell. Neurosci. 25, 263–274.

Loh, K.H., Stawski, P.S., Draycott, A.S., Udeshi, N.D., Lehrman, E.K., Wilton, D.K., Svinkina, T., Deerinck, T.J., Ellisman, M.H., Stevens, B., et al. (2016). Proteomic analysis of unbounded cellular compartments: synaptic clefts. Cell 166, 1295–1307.e21.

Loriot, S., and Cazals, F. (2010). Modeling macro-molecular interfaces with Intervor. Bioinformatics 26, 964–965.

Matsuda, K., Budisantoso, T., Mitakidis, N., Sugaya, Y., Miura, E., Kakegawa, W., Yamasaki, M., Konno, K., Uchigashima, M., Abe, M., et al. (2016). Transsynaptic modulation of kainate receptor functions by C1q-like proteins. Neuron 90, 752–767.

McCoy, A.J., Grosse-Kunstleve, R.W., Adams, P.D., Winn, M.D., Storoni, L.C., and Read, R.J. (2007). Phaser crystallographic software. J. Appl. Cryst. 40, 658–674.

Molumby, M.J., Anderson, R.M., Newbold, D.J., Koblesky, N.K., Garrett, A.M., Schreiner, D., Radley, J.J., and Weiner, J.A. (2017). γ-Protocadherins interact with neuroligin-1 and negatively regulate dendritic spine morphogenesis. Cell Rep. 18, 2702–2714.

Murshudov, G.N., Skubák, P., Lebedev, A.A., Pannu, N.S., Steiner, R.A., Nicholls, R.A., Winn, M.D., Long, F., and Vagin, A.A. (2011). REFMAC5 for the refinement of macromolecular crystal structures. Acta Crystallogr. D Biol. Crystallogr. 67, 355–367.

Myszka, D.G. (1999). Improving biosensor analysis. J. Mol. Recognit. 12, 279–284.

Nelson, S.B., and Valakh, V. (2015). Excitatory/inhibitory balance and circuit homeostasis in autism spectrum disorders. Neuron *87*, 684–698.

Perez-Garcia, C.G., and O'Leary, D.D. (2016). Formation of the cortical sub-ventricular zone requires MDGA1-mediated aggregation of basal progenitors. Cell Rep. *14*, 560–571.

Pernot, P., Round, A., Barrett, R., De Maria Antolinos, A., Gobbo, A., Gordon, E., Huet, J., Kieffer, J., Lentini, M., Mattenet, M., et al. (2013). Upgraded ESRF BM29 beamline for SAXS on macromolecules in solution. J. Synchrotron Radiat. *20*, 660–664.

Petoukhov, M.V., Franke, D., Shkumatov, A.V., Tria, G., Kikhney, A.G., Gajda, M., Gorba, C., Mertens, H.D.T., Konarev, P.V., and Svergun, D.I. (2012). New developments in the ATSAS program package for small-angle scattering data analysis. J. Appl. Cryst. *45*, 342–350.

Pettem, K.L., Yokomaku, D., Takahashi, H., Ge, Y., and Craig, A.M. (2013). Interaction between autism-linked MDGAs and neuroligins suppresses inhibitory synapse development. J. Cell Biol. *200*, 321–336.

Pettersen, E.F., Goddard, T.D., Huang, C.C., Couch, G.S., Greenblatt, D.M., Meng, E.C., and Ferrin, T.E. (2004). UCSF Chimera—a visualization system for exploratory research and analysis. J. Comput. Chem. *25*, 1605–1612.

Poulopoulos, A., Soykan, T., Tuffy, L.P., Hammer, M., Varoqueaux, F., and Brose, N. (2012). Homodimerization and isoform-specific heterodimerization of neuroligins. Biochem. J. *446*, 321–330.

Rambo, R.P., and Tainer, J.A. (2013). Accurate assessment of mass, models and resolution by small-angle scattering. Nature *496*, 477–481.

Reeves, P.J., Callewaert, N., Contreras, R., and Khorana, H.G. (2002). Structure and function in rhodopsin: high-level expression of rhodopsin with restricted and homogeneous N-glycosylation by a tetracycline-inducible N-acetylglucosaminyltransferase I-negative HEK293S stable mammalian cell line. Proc. Natl. Acad. Sci. USA *99*, 13419–13424.

Reissner, C., Runkel, F., and Missler, M. (2013). Neurexins. Genome Biol. *14*, 213.

Rubenstein, J.L., and Merzenich, M.M. (2003). Model of autism: increased ratio of excitation/inhibition in key neural systems. Genes Brain Behav. *2*, 255–267.

Sauter, N.K., Grosse-Kunstleve, R.W., and Adams, P.D. (2004). Robust indexing for automatic data collection. J. Appl. Cryst. *37*, 399–409.

Savas, J.N., De Wit, J., Comoletti, D., Zemla, R., Ghosh, A., and Yates, J.R., 3rd (2014). Ecto-Fc MS identifies ligand-receptor interactions through extracellular domain Fc fusion protein baits and shotgun proteomic analysis. Nat. Protoc. *9*, 2061–2074.

Schneider, T.R., and Sheldrick, G.M. (2002). Substructure solution with SHELXD. Acta Crystallogr. D Biol. Crystallogr. *58*, 1772–1779.

Schneider, C.A., Rasband, W.S., and Eliceiri, K.W. (2012). NIH Image to ImageJ: 25 years of image analysis. Nat. Methods *9*, 671–675.

Schneidman-Duhovny, D., Hammel, M., Tainer, J.A., and Sali, A. (2013). Accurate SAXS profile computation and its assessment by contrast variation experiments. Biophys. J. *105*, 962–974.

Schreiner, D., Nguyen, T.M., Russo, G., Heber, S., Patrignani, A., Ahrné, E., and Scheiffele, P. (2014). Targeted combinatorial alternative splicing generates brain region-specific repertoires of neurexins. Neuron *84*, 386–398.

Schrodinger, L.L.C. (2010). The PyMOL Molecular Graphics System. https://www.pymol.org/.

Siddiqui, T.J., and Craig, A.M. (2011). Synaptic organizing complexes. Curr. Opin. Neurobiol. *21*, 132–143.

Siddiqui, T.J., Pancaroglu, R., Kang, Y., Rooyakkers, A., and Craig, A.M. (2010). LRRTMs and neuroligins bind neurexins with a differential code to cooperate in glutamate synapse development. J. Neurosci. *30*, 7495–7506.

Singh, S.K., Stogsdill, J.A., Pulimood, N.S., Dingsdale, H., Kim, Y.H., Pilaz, L.J., Kim, I.H., Manhaes, A.C., Rodrigues, W.S., Jr., Pamukcu, A., et al. (2016). Astrocytes assemble thalamocortical synapses by bridging NRX1α and NL1 via hevin. Cell *164*, 183–196.

Song, J.Y., Ichtchenko, K., Südhof, T.C., and Brose, N. (1999). Neuroligin 1 is a postsynaptic cell-adhesion molecule of excitatory synapses. Proc. Natl. Acad. Sci. USA *96*, 1100–1105.

Südhof, T.C. (2008). Neuroligins and neurexins link synaptic function to cognitive disease. Nature *455*, 903–911.

Tabuchi, K., Blundell, J., Etherton, M.R., Hammer, R.E., Liu, X., Powell, C.M., and Südhof, T.C. (2007). A neuroligin-3 mutation implicated in autism increases inhibitory synaptic transmission in mice. Science *318*, 71–76.

Takeuchi, A., and O'Leary, D.D. (2006). Radial migration of superficial layer cortical neurons controlled by novel Ig cell adhesion molecule MDGA1. J. Neurosci. *26*, 4460–4464.

Takeuchi, A., Hamasaki, T., Litwack, E.D., and O'Leary, D.D. (2007). Novel IgCAM, MDGA1, expressed in unique cortical area- and layer-specific patterns and transiently by distinct forebrain populations of Cajal-Retzius neurons. Cereb. Cortex *17*, 1531–1541.

Tanaka, H., Miyazaki, N., Matoba, K., Nogi, T., Iwasaki, K., and Takagi, J. (2012). Higher-order architecture of cell adhesion mediated by polymorphic synaptic adhesion molecules neurexin and neuroligin. Cell Rep. *2*, 101–110.

Taniguchi, H., Gollan, L., Scholl, F.G., Mahadomrongkul, V., Dobler, E., Limthong, N., Peck, M., Aoki, C., and Scheiffele, P. (2007). Silencing of neuroligin function by postsynaptic neurexins. J. Neurosci. *27*, 2815–2824.

Terwilliger, T.C., Adams, P.D., Read, R.J., McCoy, A.J., Moriarty, N.W., Grosse-Kunstleve, R.W., Afonine, P.V., Zwart, P.H., and Hung, L.W. (2009). Decision-making in structure solution using Bayesian estimates of map quality: the PHENIX AutoSol wizard. Acta Crystallogr. D Biol. Crystallogr. *65*, 582–601.

Uemura, T., Lee, S.J., Yasumura, M., Takeuchi, T., Yoshida, T., Ra, M., Taguchi, R., Sakimura, K., and Mishina, M. (2010). Trans-synaptic interaction of GluRdelta2 and neurexin through Cbln1 mediates synapse formation in the cerebellum. Cell *141*, 1068–1079.

Ullrich, B., Ushkaryov, Y.A., and Südhof, T.C. (1995). Cartography of neurexins: more than 1000 isoforms generated by alternative splicing and expressed in distinct subsets of neurons. Neuron *14*, 497–507.

Varoqueaux, F., Jamain, S., and Brose, N. (2004). Neuroligin 2 is exclusively localized to inhibitory synapses. Eur. J. Cell Biol. *83*, 449–456.

Varoqueaux, F., Aramuni, G., Rawson, R.L., Mohrmann, R., Missler, M., Gottmann, K., Zhang, W., Südhof, T.C., and Brose, N. (2006). Neuroligins determine synapse maturation and function. Neuron *51*, 741–754.

Walter, T.S., Diprose, J.M., Mayo, C.J., Siebold, C., Pickford, M.G., Carter, L., Sutton, G.C., Berrow, N.S., Brown, J., Berry, I.M., et al. (2005). A procedure for setting up high-throughput nanolitre crystallization experiments. Crystallization workflow for initial screening, automated storage, imaging and optimization. Acta Crystallogr. D Biol. Crystallogr. *61*, 651–657.

Walter, T.S., Mancini, E.J., Kadlec, J., Graham, S.C., Assenberg, R., Ren, J., Sainsbury, S., Owens, R.J., Stuart, D.I., Grimes, J.M., and Harlos, K. (2008). Semi-automated microseeding of nanolitre crystallization experiments. Acta Crystallogr. Sect. F Struct. Biol. Cryst. Commun. *64*, 14–18.

Webb, B., and Sali, A. (2014). Comparative protein structure modeling using MODELLER. Curr. Protoc. Bioinformatics *47*, 1–32.

Weinkam, P., Pons, J., and Sali, A. (2012). Structure-based model of allostery predicts coupling between distant sites. Proc. Natl. Acad. Sci. USA *109*, 4875–4880.

Winter, G., Lobley, C.M., and Prince, S.M. (2013). Decision making in xia2. Acta Crystallogr. D Biol. Crystallogr. *69*, 1260–1273.

Xu, J., Xiao, N., and Xia, J. (2010). Thrombospondin 1 accelerates synaptogenesis in hippocampal neurons through neuroligin 1. Nat. Neurosci. *13*, 22–24.

Xu, X., Xiong, Z., Zhang, L., Liu, Y., Lu, L., Peng, Y., Guo, H., Zhao, J., Xia, K., and Hu, Z. (2014). Variations analysis of NLGN3 and NLGN4X gene in Chinese autism patients. Mol. Biol. Rep. *41*, 4133–4140.

# STAR★METHODS

## KEY RESOURCES TABLE

| REAGENT or RESOURCE | SOURCE | IDENTIFIER |
|---|---|---|
| **Antibodies** | | |
| Anti-c-myc, rabbit polyclonal | Sigma-Aldrich | Cat# C3956; RRID: AB_439680 |
| Anti-HA, mouse monoclonal IgG2b | Roche | Cat# 11583816001; RRID: AB_514505 |
| Anti-synapsin1, mouse monoclonal IgG1 | Synaptic Systems | Cat # 106011 |
| Anti-tau, mouse monoclonal IgG2a | Millipore | Cat# MAB3420; RRID: AB_94855 |
| Anti-V5, mouse monoclonal IgG2a | Thermo Fisher | Cat# R960-25; RRID: AB_2556564 |
| AMCA goat anti-rabbit IgG (H+L) | Jackson ImmunoResearch | Cat# 111-155-144; RRID: AB_2337994 |
| Alexa Fluor 488 goat anti-rabbit IgG (H+L) | Thermo Fisher | Cat# R37116; RRID: AB_2556544 |
| Alexa Fluor 488 goat anti-mouse IgG2b | Thermo Fisher | Cat# A-21141; RRID: AB_2535778 |
| Alexa Fluor 568 goat anti-mouse IgG1 | Thermo Fisher | Cat# A-21124; RRID: AB_2535766 |
| Alexa Fluor 647 goat anti-mouse IgG2a | Thermo Fisher | Cat# A-21241; RRID: AB_2535810 |
| Streptavidin-HRP conjugate | Sigma-Aldrich | Cat# GERPN1231 |
| **Chemicals, Peptides, and Recombinant Proteins** | | |
| Neurobasal Medium | Thermo Fisher | Cat# 21103049 |
| GlutaMAX | Thermo Fisher | Cat# 35050061 |
| B27 serum-free supplement | Thermo Fisher | Cat# 17504044 |
| APV | Abcam | Cat# ab120271 |
| Dulbecco's Modified Eagle Medium, high glucose | Sigma-Aldrich | Cat# D5796 |
| Dulbecco's Modified Eagle Medium, high glucose, no L-Methionine | Sigma-Aldrich | Cat# D0422 |
| Bovine growth serum | GE Healthcare | Cat# SH30541.03 |
| Penicillin/streptomycin | Thermo Fisher | Cat# 15070063 |
| TransIT-LT1 transfection reagent | Mirus Bio | Cat# MIR2305 |
| Pyrobest DNA Polymerase | Takara | Cat# R005A |
| Seleno-L-Methionine | Sigma-Aldrich | Cat# S3132 |
| D-biotin | Sigma-Aldrich | Cat# B4639 |
| Streptavidin | Sigma-Aldrich | Cat# S4762 |
| Bovine serum albumin | Sigma-Aldrich | Cat# A7638 |
| Polyethylenimine, branched | Sigma-Aldrich | Cat# 408727 |
| Ammonium bicarbonate | Sigma-Aldrich | Cat# 09830 |
| Urea | Thermo Scientific | Cat# 29700 |
| Tris(2-carboxyethyl)phosphine hydrochloride (TCEP) | Sigma-Aldrich | Cat# C4706 |
| Iodoacetamide | Sigma-Aldrich | Cat# I1149 |
| Pierce Trypsin Protease, MS Grade | Thermo Scientific | Cat# 90057 |
| ProteaseMAX Surfactant, Trypsin Enhancer | Promega | Cat# V2072 |
| Formic Acid Optima LC/MS | Thermo Fisher | Cat# A117 |
| Trifluoroacetic Acid (TFA) | Thermo Fisher | Cat# O4902 |
| Acetonitrile Optima LC/MS | Thermo Fisher | Cat# A955 |
| **Deposited Data** | | |
| hNL1(–A+B)$_{ECTO}$ | This paper | PDB: 5OJK |
| cMDGA1$_{ECTO}$ | This paper | PDB: 5OJ2 |
| hNL1$_{ECTO}$–cMDGA1$_{ECTO}$ | This paper | PDB: 5OJ6 |

*(Continued on next page)*

*Continued*

| REAGENT or RESOURCE | SOURCE | IDENTIFIER |
|---|---|---|
| Experimental Models: Cell Lines | | |
| COS-7 | ATCC | Cat# CRL-1651; RRID: CVCL_0224 |
| HEK293T | ATCC | Cat# CRL-3216; RRID: CVCL_0063 |
| HEK293S GnTI$^{-/-}$ | ATCC | Cat# CRL-3022; RRID: CVCL_A785 |
| Experimental Models: Organisms/Strains | | |
| Sprague Dawley rat, female timed pregnant d18 | Charles River Canada | Strain code 400 |
| Software and Algorithms | | |
| MetaMorph | Molecular Devices | https://www.moleculardevices.com/systems/metamorph-research-imaging/metamorph-microscopy-automation-and-image-analysis-software |
| ImageJ | Schneider et al., 2012 | https://imagej.nih.gov/ij/download.html |
| GraphPad Prism | GraphPad Software | http://www.graphpad.com/scientific-software/prism/ |
| SHELXD | Schneider and Sheldrick, 2002 | http://shelx.uni-ac.gwdg.de/SHELX/ |
| Phenix | Adams et al., 2010 | https://www.phenix-online.org/ |
| XIA2 | Winter et al., 2013 | http://xds.mpimf-heidelberg.mpg.de/ |
| PISA | Krissinel and Henrick, 2007 | http://www.ebi.ac.uk/pdbe/pisa/ |
| Intervor | Loriot and Cazals, 2010 | N/A |
| Coot | Emsley et al., 2010 | http://www2.mrc-lmb.cam.ac.uk/personal/pemsley/coot/ |
| PyMOL | Schrodinger, 2010 | https://www.pymol.org/ |
| BLAST | Altschul et al., 1990 | https://blast.ncbi.nlm.nih.gov/ |
| MUSCLE | Edgar, 2004 | http://www.ebi.ac.uk/Tools/msa/muscle/ |
| ALINE | Bond and Schüttelkopf, 2009 | http://bondxray.org/software/aline.html |
| Consurf | Ashkenazy et al., 2010 | http://consurf.tau.ac.il/2016/ |
| ATSAS | Petoukhov et al., 2012 | https://www.embl-hamburg.de/biosaxs/software.html |
| ScÅtter | Rambo and Tainer, 2013 | http://www.bioisis.net/ |
| SWISS-MODEL | Biasini et al., 2014 | https://swissmodel.expasy.org/ |
| MODELER | Webb and Sali, 2014 | https://salilab.org/modeller/ |
| UCSF CHIMERA | Pettersen et al., 2004 | https://www.cgl.ucsf.edu/chimera/ |
| AllosMod-FoXS | Guttman et al., 2013 | http://modbase.compbio.ucsf.edu/allosmod-foxs/ |
| Scrubber2 | BioLogic Software | http://www.biologic.com.au/ |
| BIAevaluation | GE Healthcare | https://www.biacore.com/ |
| Origin ITC | Malvern | https://www.malvern.com/en/ |
| Sedfit | Brown and Schuck, 2006 | http://www.analyticalultracentrifugation.com/default.htm |
| GUSSI | Brautigam, 2015 | http://biophysics.swmed.edu/MBR/software.html |
| Integrated Proteomics Pipeline | Savas et al., 2014 | http://www.integratedproteomics.com/ |
| Other | | |
| HisTrap FF | GE Healthcare | Cat# 17-5255-01 |
| Superdex 16/60 200 PG HiLoad | GE Healthcare | Cat# 28989335 |
| QuixStand | GE Healthcare | Cat# 56-4107-78 |
| Biacore T200 | GE Healthcare | Cat# 28975001 |
| Sensor Chip CM5 | GE Healthcare | Cat# BR100012 |
| EASY-nLC 1000 Liquid Chromatograph | Thermo Scientific | Cat# LC120 |
| Orbitrap Fusion Tribrid Mass Spectrometer | Thermo Scientific | Cat# IQLAAEGAAPFADBMBCX |
| Acclaim PepMap 100 75 um x 2 cm nanoViper | Thermo Scientific | Cat# 164946 |
| Acclaim PepMap RSLC 75 um x 50 cm nanoViper | Thermo Scientific | Cat# 164942 |

## CONTACT FOR REAGENT AND RESOURCE SHARING

Further information and requests for reagents may be directed to and will be fulfilled by the Lead Contact, A. Radu Aricescu (radu@mrc-lmb.cam.ac.uk).

## METHOD DETAILS

### Expression and purification of recombinant proteins

List of cDNAs and construct boundaries for secreted protein production: chicken MAM domain-containing glycosylphosphatidylinositol anchor protein (MDGA) 1 (MDGA1; GenBank: AB241390.1; Gln19-Lys919), human MDGA1 (GenBank: NM_153487.3; Gln19-Lys925), human MDGA2 (GenBank: AY369208.1; Gln21-Lys927), human neuroligin-1 (NL1; GenBank: NM_014932.3; Gln46-Asp635), human neuroligin-2 (NL2; GenBank: NM_020795.3; Glu38-His612), human neuroligin-3 (NL3; GenBank: NM_181303; Gln38-Asp636), human neuroligin-4 (NL4 or NL4(X); GenBank: NM_020742.3; Gln42-Glu602), human neuroligin-5 (NL5 or NL4(Y); GenBank: NM_014893.4; Gln42-Glu602), human β-neurexin-1 (GenBank: NM_138735; β-NRX1: His85-Val265), human thrombospondin-1 (TSP1; GenBank: X04665.1; Asn19-Pro1170), human hevin (or SPARC-like protein 1; GenBank: BC033721.1; Ile17-Phe664), mouse α-Neurexin-1 (GenBank: XM_006523816.3; Leu31-Val1337).

These cDNAs were fused C-terminally with a hexa-histidine (His6) tag or Avitag3, and were cloned into the pHLsec vector (Aricescu et al., 2006b). For large-scale protein production, His6-tagged proteins were expressed by transient transfection in HEK293T (for biophysical studies) or HEK293S-GnTI$^{-/-}$ (Reeves et al., 2002) (for crystallographic studies) cells. Five (HEK293T) to ten (HEK293S-GnTI$^{-/-}$) days post-transfection, the conditioned Dulbecco's Modified Eagle Medium (DMEM) medium was collected and buffer-exchanged using a QuixStand benchtop diafiltration system (GE Healthcare) and proteins were purified by immobilized metal-affinity chromatography (IMAC) using pre-packed Nickel Sepharose columns (GE Healthcare). Proteins were concentrated and further purified by size-exclusion chromatography (SEC; Superdex 200 16/60 PG HiLoad column, GE Healthcare) in 10 mM HEPES (4-(2-hydroxyethyl)-1-piperazineethanesulfonic acid) pH 7.50, 150 mM sodium chloride and 3 mM calcium chloride (HBS-C).

### Expression and purification of recombinant NMDA receptor

The rat GluN1a-GluN2B heterotetrameric NMDA receptor (NMDAR) was expressed and purified as previously described (Karakas and Furukawa, 2014), with the exception that the OneStrep tag was not cleaved. The final purification buffer was 200 mM NaCl, 20 mM HEPES pH 7.4, 10 mM Glycine, 10 mM Glutamate, 0.0025% LMNG.

### Gene splicing and site-directed mutagenesis

A multiple-step overlap-extension PCR (Pyrobest Polymerase, Takara Bio) was used for site-directed mutagenesis, construction of chimeric protein constructs and introduction or deletion of splice inserts (Heckman and Pease, 2007); the resulting PCR products were cloned into the pHLsec-His6, pHLsec-Avitag3, or derived vectors (Aricescu et al., 2006b).

#### *NL1*

The following internal primer pair was used for the introduction of human NL1 spliced sequence "A1" (VKRISKECARKPGKKICRKG) into human NL1(–A ± B) (UniProt: Q8N2Q7; between Asp164 and Asp182);

    FP: 5′-CCAAGGAATGTGCCAGAAAGCCCGGCAAGAAAATATGTAGAAAAGGAGATATTCGGGACAGTGGGGGGTCCCAAACCAG-3′
    RP: 5′-CTTGCCGGGCTTTCTGGCACATTCCTTGGATATTCTTTTTACATCCTCAGTCGGGACATATATATTTAAATATAG-3′

The following internal primer pair was used for the introduction of human NL1 spliced sequence "A2" (GPLTKKQTDD LGDNDGAEDE) into human NL1(–A ± B) (between Asp164 and Asp182);

    FP: 5′-GAAACAGACAGATGATTTAGGTGATAATGACGGTGCTGAAGATGAAGATATTCGGGACAGTGGGGGGTCCCAAACCAG-3′
    RP: 5′-CTTGCCGGGCTTTCTGGCACATTCCTTGGATATTCTTTTTACATCCTCAGTCGGGACATATATATTTAAATATAG-3′

The following internal primer pair was used for the introduction of human NL1 spliced sequence "A2" (GPLTKKQTDDL GDNDGAEDE) into human NL1(+A1 ± B) (after spliced sequence A1);

    FP: 5′-GAAACAGACAGATGATTTAGGTGATAATGACGGTGCTGAAGATGAAGATATTCGGGACAGTGGGGGGTCCCAAACCAG-3′
    RP: 5′-CATTATCACCTAAATCATCTGTCTGTTTCTTTGTAAGGGGACCTCCTTTTCTACATATTTTCTTGCCGGGCTTTC-3′

The following internal primer pair was used for the introduction of human NL1 spliced sequence "B" (NRWSNSTKG) into human NL1(±A–B) (between Gly295 and Leu305);

    FP: 5′-GTAACCGTTGGAGCAATTCAACCAAAGGACTTTTTCAACGAGCAATAGCTCAAAG-3′
    RP: 5′-GTCCTTTGGTTGAATTGCTCCAACGGTTACCTTCAGAATAATGGGATAAAGTC-3′

The following internal primer pairs were used for constructing the human NL1 ΔSite I mutant (H291A-Y292A-D384A-E394A);

H291A Y292A (LTLS<u>HY</u>SEGL to LTLS<u>AA</u>SEGL);

    FP: 5′-GTCAACCTGCTGACTTTATCCGCTGCTTCTGAAGGTCTTTTTCAACGAG-3′
    RP: 5′-CTCGTTGAAAAAGACCTTCAGAAGCAGCGGATAAAGTCAGCAGGTTGAC-3′

D384A (VIP<u>D</u>DPQI to VIP<u>A</u>DPQI);

    FP: 5′-GGT<u>G</u>ATGTAATACCAGCCGACCCCCAGATATTG-3′
    RP: 5′-CAATATCTGGGGGTCGGCTGGTATTACATCACC-3′

E394A (MEQGEFLNY to MEQGAFLNY);

    FP: 5′-GATGGAGCAAGGAGCGTTTCTCAACTATG-3′

    RP: 5′-CATAGTTGAGAAACGCTCCTTGCTCCATC-3′

The following internal primer pairs were used for constructing the human NL1 ΔSite II mutant (D429A-F430A-S433A-N434A-R450A);

    D429A F430A S433A N434A (ASDFDFAVSNFVDN to ASDFAAAVAAFVDN);

    FP: 5′-GCCGCTGCTGTTGCAGCTTTTGTTGATAATTTATATGGATATCCTGAAGGCAAAGATG-3′

    RP: 5′-AGCTGCAACAGCAGCGGCAAAATCACTAGCTGATATACCATCATCGCTATCTAC-3′

    R450A (KDVLRETIK to KDVLAETIK);

    FP: 5′-GAAGGCAAAGATGTTTTGGCAGAAACCATTAAGTTCATG-3′

    RP: 5′-CATGAACTTAATGGTTTCTGCCAAAACATCTTTGCCTTC-3′

The following internal primer pair was used for introducing the R450C mutation into human NL1(–A–B) (DVLRETI to DVLCETI);

    FP: 5′-GGCAAAGATGTTTTGTGCGAAACCATTAAGTTC-3′

    RP: 5′-GAACTTAATGGTTTCGCACAAAACATCTTTGCC-3′

The following internal primer pair was used for introducing the Asn300Gln (N300Q) mutation into human NL1 spliced sequence "B" (NRWSNSTKG to NRWSQSTKG);

    FP: 5′-GGTAACCGTTGGAGCCAGTCAACCAAAGGAC-3′

    RP: 5′-GTCCTTTGGTTGACTGGCTCCAACGGTTACC-3′

### NL2

The following internal primer pair was used for the introduction of human NL2 spliced sequence "A" (GPLTKKRDEATLNPPDT) into human NL2(–A) (UniProt: Q8NFZ4; between Asp152 and Asp170);

    FP: 5′-CACAAAAAAACGTGACGAGGCGACGCTCAATCCGCCAGACACAGATATCCGGGACCCTGGGAAGAAACCTGTC-3′

    RP: 5′-GATTGAGCGTCGCCTCGTCACGTTTTTTTTGTGAGCGGACCGTCCTCAGTGGGCACGTAGAGGTTGAGGTAC-3′

### NL3

The following internal primer pair was used for the introduction of human NL3 spliced sequence "A1" (VKRISKECARKPNKKICRKG) into human NL3(–A) (UniProt: Q9NZ94; between Asp152 and Asp193);

    FP: 5′-CCAAGGAATGCGCCCGAAAGCCCAACAAGAAAATTTGTAGGAAAGGAGACATCCGGGACAGTGGTGCTAAACCCGTC-3′

    RP: 5′-GTTGGGCTTTCGGGCGCATTCCTTGGAAATCCGCTTTACATCCTCCGTCGGCACATAGACGTTCAGGTAG-3′

The following internal primer pair was used for the introduction of human NL3 spliced sequence "A2" (GSGAKKQGEDLADNDG DEDE) into human NL3(–A) (between Asp152 and Asp193);

    FP: 5′-GAAACAGGGCGAGGACTTAGCGGATAATGACGGGGATGAAGATGAAGACATCCGGGACAGTGGTGCTAAACCCGTC −3′

    RP: 5′-CCGCTAAGTCCTCGCCCTGTTTCTTAGCGCCGGATCCATCCTCCGTCGGCACATAGACGTTC-3′

The following internal primer pair was used for the introduction of human NL3 spliced sequence "A2" (GSGAKKQGEDLADNDG DEDE) into human NL3(+A1) (after spliced sequence A1);

    FP: 5′-GAAACAGGGCGAGGACTTAGCGGATAATGACGGGGATGAAGATGAAGACATCCGGGACAGTGGTGCTAAACCCGTC-3′

    RP: 5′-CATTATCCGCTAAGTCCTCGCCCTGTTTCTTAGCGCCGGATCCTCCTTTCCTACAAATTTTCTTGTTGGGCTTTC-3′

The following internal primer pair was used for introducing the R451C mutation into human NL3(–A) (DTLRETI to DTLCETI);

    FP: 5′-GGTAAGGACACCCTGTGCGAGACCATCAAGTTC-3′

    RP: 5′-GAACTTGATGGTCTCGCACAGGGTGTCCTTACC-3′

### MDGA1

The following internal primer pair was used for introducing the R120K mutation into chicken MDGA1 (UniProt: Q0WYX8; VPAIRSIRV to VPAIKSIRV);

    FP: 5′-GTTGGGGTCCCTGCCATCAAGTCCATTCGAGTAGATGTGCAG-3′

    RP: 5′-CTGCACATCTACTCGAATGGACTTGATGGCAGGGACCCCAAC-3′

The following internal primer pairs were used for constructing the chicken MDGA1 R156N-S502N-R680N glycan wedge mutant;

    R156N (TVFLRCTVN to TVFLNCTVN);

    FP: 5′-GAGAAGACTGTCTTCCTCAATTGTACCGTCAACTCCAAC-3′

    RP: 5′-GTTGGAGTTGACGGTACAATTGAGGAAGACAGTCTTCTC-3′

    S502N (LRLESVSRD to LRLENVSRD);

    FP: 5′-GGAAGCTGCGCCTGGAGAATGTCAGCCGAGACATGAG-3′

    RP: 5′-CTCATGTCTCGGCTGACATTCTCCAGGCGCAGCTTCC-3′

    R680N (LAQRNTIQ to LAQNNTIQ);

    FP: 5′-GTCAGGCAGCTGGCTCAGAACAACACCATCCAAACCTTC-3′

    RP: 5′-GAAGGTTTGGATGGTGTTGTTCTGAGCCAGCTGCCTGAC-3′

### β-NRX1

The following internal primer pair was used for the introduction of human β-NRX1 spliced sequence #4 (SS4; GNNDNERLAIARQRIPYRLGRVVDEWLLDK) into human β-NRX1(–4) (UniProt: P58400; between Ala204 and Gly205);

    FP: 5′-CGCATTCCCTATCGGCTAGGGAGAGTGGTGGACGAATGGCTGCTCGATAAAGGGAGGCAACTGACCATCTTCAACTCAC-3′

    RP: 5′-CCCTAGCCGATAGGGAATGCGTTGCCGTGCTATGGCTAACCTCTCATTGTCGTTGTTTCCAGCTGGGTATCTCTCAATGAC-3′

### TSP1

The following internal primer pair was used for introducing the C992S mutation (Kvansakul et al., 2004) into human TSP1 (UniProt: P07996; QTVNCDPGL to QTVNSDPGL);

FP: 5′-CAGACTGTCAACAGTGATCCTGGACTC-3′
RP: 5′-GAGTCCAGGATCACTGTTGACAGTCTG-3′

### Protein crystallization

Crystallization trials, using 100 nL protein solution plus 100 nL reservoir solution in sitting drop vapor diffusion format, were set up in 96-well Greiner plates using a Cartesian Technologies robot (Walter et al., 2005).

Purified chicken MDGA1$_{ECTO}$ (cMDGA1$_{ECTO}$; Gln19-Lys919), containing the Arg120Lys mutation, concentrated to 5.0 g/L and treated with endoglycosidase F1 (Endo F1; 1:100 w/w) for 30 min at 294K immediately prior to dispensing the crystallization drops, crystallized in 0.1M HEPES pH7.5, 4% w/v polyethylene glycol 8000. The Arg120Lys mutation was introduced into cMDGA1$_{ECTO}$ to bring the sequence in line with rat, mouse and human isoforms (Figure S1B).

Crystals of cMDGA1$_{ECTO}$ grown in this condition were fragmented, and the obtained seed stock (Walter et al., 2008) was used as an additive during crystallization trials of selenomethionine- (SeMet) labeled cMDGA1$_{ECTO}$. Matrix screens were performed using precipitant concentration and seed stock dilution as variables. SeMet-labeled cMDGA1$_{ECTO}$, concentrated to 5.0 g/L, crystallized in 0.1M HEPES pH7.5, 3% w/v polyethylene glycol 8000, using a 32-fold diluted native cMDGA1$_{ECTO}$ seed stock dispensed in 20 nL drops. Crystals were cryoprotected using reservoir solution containing 20% (v/v) PEG200.

Purified glycosylated human NL1(–A+B)$_{ECTO}$ (hNL1(–A+B)$_{ECTO}$; Gln46-Asp635), concentrated to 10.0 g/L, crystallized in 0.2M KSCN, 0.1M Bis-tris propane pH 8.5, 20% w/v PEG3350. Crystals were cryoprotected using reservoir solution containing 20% (v/v) PEG200.

To crystallize the hNL1(–A–B)$_{ECTO}$–cMDGA1$_{ECTO}$ complex, purified hNL1(–A–B)$_{ECTO}$ (Gln46-Asp635; concentrated to 2.92 g/L = 45.30 μM) and cMDGA1$_{ECTO}$ (Gln19-Lys919 with Arg120Lys mutation; concentrated to 4.41 g/L = 42.94 μM) were mixed as follows; 80 μL hNL1(–A–B)$_{ECTO}$ was combined with 102 μL cMDGA1$_{ECTO}$ (resulting in a 1:1.25 NL1:MDGA1 monomer-to-monomer molar stoichiometric ratio), 18 μL purification buffer (10 mM HEPES pH7.5, 150 mM NaCl), and 50 μL dilution buffer (10 mM HEPES pH7.5, 150 mM NaCl, 1M NDSB-256). The final concentration of hNL1(–A–B)$_{ECTO}$ thus was 0.93 g/L; that of cMDGA1$_{ECTO}$ was 1.76 g/L; and that of NDSB-256 was 250 mM. This preparation was treated with endoglycosidase F1 (Endo F1; 1:100 w/w) for 30 min at 294K immediately prior to dispensing the crystallization drops. The hNL1(–A–B)$_{ECTO}$–cMDGA1$_{ECTO}$ complex crystallized in 0.1M Na.HEPES pH 7.0, 7.5% w/v PEG8000. Crystals were cryoprotected using reservoir solution containing 33% (v/v) PEG200.

### Crystallographic data collection and structure determination

Diffraction data for cMDGA1$_{ECTO}$ were collected at Diamond Light Source (DLS) beamline I03 to a nominal resolution of 3.20 Å in space group (SG) $P2_12_12_1$. X-ray fluorescence wavelength scans were performed to experimentally determine the Selenium absorption K-edge peak. The cMDGA1$_{ECTO}$ structure was determined using Single Anomalous Diffraction (SAD); the heavy-atom Selenium substructure was solved using SHELXD (Schneider and Sheldrick, 2002) at 3.70 Å, and phase determination, phase extension and density modification was performed using PHENIX Autosol (Terwilliger et al., 2009). Automated model building programs failed to reliably place stretches of β strand, necessitating manual model building of the complete structure.

Diffraction data for hNL1(–A+B)$_{ECTO}$ were collected at Diamond Light Source (DLS) beamline I24 to a nominal resolution of 2.55 Å in SG $P22_12_1$. The structure was determined by molecular replacement using the program Phaser (McCoy et al., 2007), and using the mouse NL1 (PDB: 3BIX) crystal structure as search model.

Diffraction data for the hNL1(–A–B)$_{ECTO}$–cMDGA1$_{ECTO}$ complex were collected at Diamond Light Source (DLS) beamline I04-1 to a nominal resolution of 3.30 Å in SG $P2_12_12$. The structure was determined by molecular replacement using the program Phaser (McCoy et al., 2007), employing the refined hNL1(–A+B)$_{ECTO}$ (in which the spliced sequence B was excised from the molecular model) and cMDGA1$_{ECTO}$ crystal structures we determined here as search models.

All data were indexed, integrated, and scaled using the automated XIA2 expert system (Winter et al., 2013), using the Labelit (Sauter et al., 2004), POINTLESS and AIMLESS (Evans, 2006, 2011), and XDS (Kabsch, 2010) programs. Crystallographic data collection and refinement statistics are presented in Table S1.

### Crystallographic refinement and model analysis

Maximum-likelihood refinement of cMDGA1$_{ECTO}$, hNL1(–A+B)$_{ECTO}$ and the hNL1(–A–B)$_{ECTO}$–cMDGA1$_{ECTO}$ complex was initially performed with Refmac using "jelly body" restraints (Murshudov et al., 2011), and finally with the PHENIX suite (Adams et al., 2010), with automated X-ray and atomic displacement parameter (ADP) weight optimization applied throughout, and torsion angle non-crystallographic symmetry (NCS) and high-resolution reference structure restraints applied where suitable. All manual model building was performed using Coot (Emsley et al., 2010). Structure validation was performed with the PHENIX program suite using MolProbity routines (Adams et al., 2010; Chen et al., 2010).

Interface analysis was performed using PISA (Krissinel and Henrick, 2007) as implemented in Coot (Emsley et al., 2010), and using the program Intervor (Loriot and Cazals, 2010). Calculation of pairwise root-mean-square deviations (rmsd) between structural model

coordinates was performed using the program PyMol (Schrodinger, 2010). Molecular representations were made using the program PyMol (Schrodinger, 2010).

## Sequence alignments and conservation analysis

Mining of protein sequence databases was performed using the Delta-Blast program (Altschul et al., 1990). Sequence lists were manually curated and sequences were aligned using the program MUSCLE (Edgar, 2004). Sequence conservation scores for individual residue positions of NL1, −2, −3, −4, and −5 (1046 total unique sequences) and MDGA1 and −2 (420 total unique sequences) homologs were assigned to NL1 and MDGA1 structural templates extracted from the hNL1(−A−B)$_{ECTO}$−cMDGA1$_{ECTO}$ complex, respectively, using the ConSurf web server (Ashkenazy et al., 2010). Sequence alignments were visualized using the program ALINE (Bond and Schüttelkopf, 2009).

## Small-angle X-ray scattering (SAXS)

Purified cMDGA1$_{ECTO}$ (Gln19-Lys919; with Arg120Lys mutation) was treated with endoglycosidase F1 (Endo F1; 1:100 w/w) for 12 hr at 294K and re-purified using SEC in 10 mM HEPES pH 7.50, 150 mM NaCl. SAXS data were collected at beamline BM29 of the European Synchrotron Radiation Facility (ESRF, Grenoble, France) (Pernot et al., 2013) at 293 K within a momentum transfer ($q$) range of 0.01 Å$^{-1}$ < $q$ < 0.45 Å$^{-1}$, where $q = 4\pi\sin(\theta)/\lambda$, and $2\theta$ is the scattering angle. The X-ray wavelength was 0.9950 Å, and data were collected on a Pilatus 1M detector. cMDGA1$_{ECTO}$ was measured at concentrations of 1.50 and 3.36 g/L in 10 mM HEPES pH 7.50, 150mM NaCl. Data reduction and calculation of invariants was carried out using standard procedures implemented in the ATSAS (Petoukhov et al., 2012) and ScÅtter (Rambo and Tainer, 2013) suites. A merged dataset was obtained by merging the low-angle part of the low-concentration dataset with the high-angle part of the high-concentration dataset.

A molecular model for the C-terminal Mam$_8$ domain was generated by homology modeling starting from the crystal structure of the N-terminal RPTPmu MAM domain (PDB: 2C9A, UniProt: P28827) (Aricescu et al., 2006a) using the SWISS-MODEL server (Biasini et al., 2014). This model was concatenated with the cMDGA1$_{ECTO}$ crystal structure, and manually placed near the C terminus of the FnIII$_7$ domain. Missing side chains, loops, and C-terminal His6-tag were added to the resulting assembled model using the MODELER (Webb and Sali, 2014) "Model/Refine Loops" routine as implemented in Chimera (Pettersen et al., 2004).

Coarse-grained molecular dynamics (MD) simulations were performed using the program Allosmod (Weinkam et al., 2012). Five independent runs were performed, each consisting of 30 independent trajectories generating 100 models. From this total pool of 15,000 models, automated selection of the minimal set of models that best described the scattering data was performed with the program MES (Hammel, 2012), and calculation and fitting of scattering patterns were performed with the program FoXS (Schneidman-Duhovny et al., 2013). This whole procedure was automated with the AllosMod-FoXS web server (Guttman et al., 2013). The MDGA1 solution structure was accurately ($\chi^2 = 1.17$) modeled as a five-membered ensemble of monomeric conformers with pronounced flexibility at the FnIII$_7$-Mam$_8$ domain linkage.

## Surface plasmon resonance (SPR) with soluble proteins

cDNA for the immobilized proteins was cloned into the pHLsec-Avitag3 vector (Aricescu et al., 2006b), resulting in proteins carrying a C-terminal biotin ligase (BirA) recognition sequence (Avitag). Constructs were co-transfected with pDisplay-BirA-ER (Addgene plasmid 20856; coding for an ER-resident biotin ligase) (Howarth et al., 2008) for in vivo biotinylation in HEK293T cells in small-scale 6- or 12-well plates in a 3:1 pHLsec:pDisplay stoichiometric ratio. A final concentration of 100 μM D-biotin was maintained in the expression medium to ensure near-complete biotinylation of the recognition sequence. After 48 hr of expression, conditioned medium was collected and dialysed against 10 mM Tris pH 7.4, 150 mM sodium chloride, 3 mM calcium chloride and 0.005% (v/v) Tween-20 (TBS-CT). SPR experiments were performed on a Biacore T200 machine (GE Healthcare) operated at a data collection frequency of 10 Hz; i.e. a temporal resolution of 0.1 s. Streptavidin (Sigma-Aldrich) was chemically coupled via amine coupling chemistry onto CM5 chips to a response unit (RU) level of 5000 RU. Then, biotinylated proteins were captured to the desired RU level. In each instance, for every two analyte binding cycles, a buffer injection was performed, allowing for double referencing of the binding responses (Myszka, 1999).

Due to (i) sample consumption associated with equilibrium affinity experiments of high-nanomolar to low-micromolar interactions and (ii) the limited production yield of MDGA1 and −2 proteins, we prioritized testing the full matrix of NL–MDGA isoform interactions over performing replicate experiments of only a selected number of interactions.

### *Interaction of chicken MDGA1$_{ECTO}$ with chicken MDGA1$_{ECTO}$ and MDGA1$_{ECTO}^{GLYCAN\ WEDGE}$*

cMDGA1$_{ECTO}$ and cMDGA1$_{ECTO}^{GLYCAN\ WEDGE}$ (triple glycan wedge (GW) mutant; Arg680Asn-Ser502Asn-Arg156Asn) variants were immobilized at a level of 2000 RU to maximize the likelihood of detecting a potentially weak binding event. SPR running buffer composition was TBS-CT supplemented with 1.0 g/L bovine serum albumin (BSA; yielding TBS-CTB buffer) as passivating agent to prevent binding to the carboxymethyldextran-based SPR chips. MDGA1$_{ECTO}$ was prepared by SEC in TBS-CT. BSA was added to the concentrated stock solutions to a final concentration of 1.0 g/L. Injection of 18 concentrations of cMDGA1$_{ECTO}$ prepared in a two-fold dilution series from a 100 μM stock concentration was performed in order of increasing concentration. Each sample was injected for 150 s at a flow rate of 25 μL/min, followed by a 180 s dissociation phase. No self-association binding event could be detected.

### Interaction of human β-NRX1$_{LNS6}$(–4), β-NRX1$_{LNS6}$(+4), MDGA1$_{ECTO}$ and MDGA2$_{ECTO}$ with human NL1(–A–B)$_{ECTO}$, NL2(–A)$_{ECTO}$, NL3(–A)$_{ECTO}$, NL4$_{ECTO}$ and NL5$_{ECTO}$

NL1(–A–B)$_{ECTO}$, NL2(–A)$_{ECTO}$, NL3(–A)$_{ECTO}$, NL4$_{ECTO}$ and NL5$_{ECTO}$ were immobilized at a level of 500 RU. SPR running buffer composition was TBS-CTB. β-NRX1$_{LNS6}$(–4), β-NRX1$_{LNS6}$(+4), MDGA1$_{ECTO}$ and MDGA2$_{ECTO}$ were prepared by SEC in TBS-CT. BSA was added to the concentrated stock solutions to a final concentration of 1.0 g/L. Injection of 15 concentrations of β-NRX1$_{LNS6}$(–4), β-NRX1$_{LNS6}$(+4), MDGA1$_{ECTO}$ and MDGA2$_{ECTO}$, prepared in a two-fold dilution series from a 50 μM stock concentration, was performed in order of increasing concentration. Each sample was injected for 150 s at a flow rate of 25 μL/min, followed by a 180 s dissociation phase. In the case of MDGA1$_{ECTO}$ and MDGA2$_{ECTO}$, the surfaces were regenerated using consecutive 30 s injections of 10 mM Tris pH 7.4, 100 mM L-Arginine/L-Glutamate, 1M NaCl. Equilibrium binding analysis was performed using Scrubber 2.0 (BioLogic Software) and data was fitted to a 1:1 Langmuir binding model in Prism 6 (Graphpad).

### Interaction of human NL1(–A–B)$_{ECTO}$ with human hevin, human TSP1, and mouse α-NRX1$_{ECTO}$(–4)

Human hevin, human TSP1 and mouse α-NRX1$_{ECTO}$(–4) were immobilized at a level of 2000 RU. SPR running buffer composition was TBS-CTB. Human NL1(–A–B)$_{ECTO}$ was prepared by SEC in TBS-CT. BSA was added to the concentrated stock solutions to a final concentration of 1.0 g/L. Injection of 14 concentrations of NL1(–A–B)$_{ECTO}$, prepared in a two-fold dilution series from a 25 μM stock concentration, was performed in order of increasing concentration. Each sample was injected for 150 s at a flow rate of 25 μL/min, followed by a 180 s dissociation phase. In the case of the interaction with α-NRX1$_{ECTO}$(–4), the surfaces were regenerated using a 30 s injection of 10 mM Tris pH 8.0, 350 mM EDTA, 100 mM NaCl. Equilibrium binding analysis was performed using Scrubber 2.0 (BioLogic Software) and the α-NRX1$_{ECTO}$(–4) data was fitted to a two-state Langmuir binding model in Prism 6 (Graphpad).

### Interaction of human β-NRX1$_{LNS6}$(–4), β-NRX1$_{LNS6}$(+4), MDGA1$_{ECTO}$ and MDGA2$_{ECTO}$ with human NL1(–A–B)$_{ECTO}$, NL1(–A–B)$_{ECTO}$ ΔSite I, NL1(–A–B)$_{ECTO}$ ΔSite II and NL1(–A–B)$_{ECTO}$ ΔSite I+II

NL1(–A–B)$_{ECTO}$, NL1(–A–B)$_{ECTO}$ ΔSite I, NL1(–A–B)$_{ECTO}$ ΔSite II and NL1(–A–B)$_{ECTO}$ ΔSite I+II were immobilized at a level of 550 RU. SPR running buffer composition was TBS-CTB. β-NRX1$_{LNS6}$(–4), β-NRX1$_{LNS6}$(+4), MDGA1$_{ECTO}$ and MDGA2$_{ECTO}$ were prepared by SEC in TBS-CT. BSA was added to the concentrated stock solutions to a final concentration of 1.0 g/L. Injection of 15 concentrations of β-NRX1$_{LNS6}$(–4), β-NRX1$_{LNS6}$(+4), MDGA1$_{ECTO}$ and MDGA2$_{ECTO}$, prepared in a two-fold dilution series from a 50 μM stock concentration, was performed in order of increasing concentration. Each sample was injected for 150 s at a flow rate of 25 μL/min, followed by a 180 s dissociation phase. In the case of MDGA1$_{ECTO}$ and MDGA2$_{ECTO}$, the surfaces were regenerated using consecutive 30 s injections of 10 mM Tris pH 7.4, 100 mM L-Arginine/L-Glutamate, 1M NaCl. Equilibrium binding analysis was performed using Scrubber 2.0 (BioLogic Software) and data was fitted to a 1:1 Langmuir binding model in Prism 6 (Graphpad).

### Interaction of human β-NRX1$_{LNS6}$(–4), β-NRX1$_{LNS6}$(+4), MDGA1$_{ECTO}$ and MDGA2$_{ECTO}$ with human NL1(–A–B)$_{ECTO}$, NL1(–A–B)$_{ECTO}$ Arg450Cys, NL3(–A)$_{ECTO}$, and NL3(–A)$_{ECTO}$ Arg451Cys

NL1(–A–B)$_{ECTO}$ and NL1(–A–B)$_{ECTO}$ Arg450Cys were immobilized at a level of 500 RU. NL3(–A)$_{ECTO}$ and NL3(–A)$_{ECTO}$ Arg451Cys were immobilized at a level of 1000 RU. SPR running buffer composition was TBS-CTB. β-NRX1$_{LNS6}$(–4), β-NRX1$_{LNS6}$(+4), MDGA1$_{ECTO}$ and MDGA2$_{ECTO}$ were prepared by SEC in TBS-CT. BSA was added to the concentrated stock solutions to a final concentration of 1.0 g/L. Injection of 15 concentrations of β-NRX1$_{LNS6}$(–4), β-NRX1$_{LNS6}$(+4), MDGA1$_{ECTO}$ and MDGA2$_{ECTO}$, prepared in a two-fold dilution series from a 50 μM stock concentration, was performed in order of increasing concentration. Each sample was injected for 150 s at a flow rate of 25 μL/min, followed by a 180 s dissociation phase. In the case of MDGA1$_{ECTO}$ and MDGA2$_{ECTO}$, the surfaces were regenerated using consecutive 30 s injections of 10 mM Tris pH 7.4, 100 mM L-Arginine/L-Glutamate, 1M NaCl. Equilibrium binding analysis was performed using Scrubber 2.0 (BioLogic Software) and data was fitted to a 1:1 Langmuir binding model in Prism 6 (Graphpad).

### Interaction of human β-NRX1$_{LNS6}$(–4), β-NRX1$_{LNS6}$(+4), MDGA1$_{ECTO}$ and MDGA2$_{ECTO}$ with human NL1$_{ECTO}$ SSA variants

NL1(–A–B)$_{ECTO}$, NL1(+A1–B)$_{ECTO}$, NL1(+A2–B)$_{ECTO}$ and NL1(+A1+A2–B)$_{ECTO}$ were immobilized at a level of 500 RU. SPR running buffer composition was TBS-CTB. β-NRX1$_{LNS6}$(–4), β-NRX1$_{LNS6}$(+4), MDGA1$_{ECTO}$ and MDGA2$_{ECTO}$ were prepared by SEC in TBS-CT. BSA was added to the concentrated stock solutions to a final concentration of 1.0 g/L. Injection of 15 concentrations of β-NRX1$_{LNS6}$(–4), β-NRX1$_{LNS6}$(+4), MDGA1$_{ECTO}$ and MDGA2$_{ECTO}$, prepared in a two-fold dilution series from a 50 μM stock concentration, was performed in order of increasing concentration. Each sample was injected for 150 s at a flow rate of 25 μL/min, followed by a 180 s dissociation phase. In the case of MDGA1$_{ECTO}$ and MDGA2$_{ECTO}$, the surfaces were regenerated using consecutive 30 s injections of 10 mM Tris pH 7.4, 100 mM L-Arginine/L-Glutamate, 1M NaCl. Equilibrium binding analysis was performed using Scrubber 2.0 (BioLogic Software) and data was fitted to a 1:1 Langmuir binding model in Prism 6 (Graphpad).

### Interaction of human β-NRX1$_{LNS6}$(–4), β-NRX1$_{LNS6}$(+4), MDGA1$_{ECTO}$ and MDGA2$_{ECTO}$ with human NL2$_{ECTO}$ and NL3$_{ECTO}$ SSA variants

NL2(–A)$_{ECTO}$, NL2(+A)$_{ECTO}$, NL3(–A)$_{ECTO}$, NL3(+A1)$_{ECTO}$, NL3(+A2)$_{ECTO}$ and NL3(+A1+A2)$_{ECTO}$ were immobilized at a level of 500 RU. SPR running buffer composition was TBS-CTB. β-NRX1$_{LNS6}$(–4), β-NRX1$_{LNS6}$(+4), MDGA1$_{ECTO}$ and MDGA2$_{ECTO}$ were prepared by SEC in TBS-CT. BSA was added to the concentrated stock solutions to a final concentration of 1.0 g/L. Injection of 15 concentrations of β-NRX1$_{LNS6}$(–4), β-NRX1$_{LNS6}$(+4), MDGA1$_{ECTO}$ and MDGA2$_{ECTO}$, prepared in a two-fold dilution series from a 50 μM stock concentration, was performed in order of increasing concentration. Each sample was injected for 150 s at a flow rate of 25 μL/min, followed by a 180 s dissociation phase. In the case of MDGA1$_{ECTO}$ and MDGA2$_{ECTO}$, the surfaces were regenerated using consecutive

30 s injections of 10 mM Tris pH 7.4, 100 mM L-Arginine/L-Glutamate, 1M NaCl. Equilibrium binding analysis was performed using Scrubber 2.0 (BioLogic Software) and data was fitted to a 1:1 Langmuir binding model in Prism 6 (Graphpad).

*Interaction of human $\beta$-NRX1$_{LNS6}$(–4), $\beta$-NRX1$_{LNS6}$(+4), MDGA1$_{ECTO}$ and MDGA2$_{ECTO}$ with human NL1(–A–B)$_{ECTO}$, NL1(–A+B)$_{ECTO}$, and NL1(–A+B Asn300Gln)$_{ECTO}$*

NL1(–A–B)$_{ECTO}$, NL1(–A+B)$_{ECTO}$, and NL1(–A+B Asn300Gln)$_{ECTO}$ were immobilized at a level of 500 RU. SPR running buffer composition was TBS-CTB. $\beta$-NRX1$_{LNS6}$(–4), $\beta$-NRX1$_{LNS6}$(+4), MDGA1$_{ECTO}$ and MDGA2$_{ECTO}$ were prepared by SEC in TBS-CT. BSA was added to the concentrated stock solutions to a final concentration of 1.0 g/L. Injection of 15 concentrations of $\beta$-NRX1$_{LNS6}$(–4), $\beta$-NRX1$_{LNS6}$(+4), MDGA1$_{ECTO}$ and MDGA2$_{ECTO}$, prepared in a two-fold dilution series from a 50 μM stock concentration, was performed in order of increasing concentration. Each sample was injected for 150 s at a flow rate of 25 μL/min, followed by a 180 s dissociation phase. In the case of MDGA1$_{ECTO}$ and MDGA2$_{ECTO}$, the surfaces were regenerated using consecutive 30 s injections of 10 mM Tris pH 7.4, 100 mM L-Arginine/L-Glutamate, 1M NaCl. Equilibrium binding analysis was performed using Scrubber 2.0 (BioLogic Software) and data was fitted to a 1:1 Langmuir binding model in Prism 6 (Graphpad).

## Surface plasmon resonance (SPR) with the NMDA receptor

SPR experiments were performed on a Biacore T200 machine (GE Healthcare) operated at a data collection frequency of 10 Hz; i.e. a temporal resolution of 0.1 s. Streptactin XT (IBA Lifesciences) was chemically coupled via amine coupling chemistry onto CM5 chips to a response unit (RU) level of 5000 RU. Then, OneStrep-tagged rat GluN1a-GluN2B heterotetrameric NMDA receptor (NMDAR) was captured to a level of 5000 RU. SPR running buffer composition was 200 mM NaCl, 20 mM HEPES pH 7.4, 10 mM Glycine, 10 mM Glutamate, 3mM CaCl$_2$, 0.010% LMNG. For the interaction with NL1(–A–B)$_{ECTO}$, a single-cycle kinetics (SCK) approach was adopted. Injection of 5 concentrations of NL1(–A–B)$_{ECTO}$, prepared in a two-fold dilution series from a 25 μM stock concentration, was performed in order of increasing concentration. Each sample was injected for 120 s at a flow rate of 25 μL/min, followed by a 60 s intermittent dissociation phase or a final 600 s dissociation phase.

## Isothermal titration calorimetry (ITC)

Calorimetric measurements were carried out using samples purified by SEC in HBS-C buffer (10 mM HEPES pH 7.50, 150 mM sodium chloride and 3 mM calcium chloride). Experiments were carried out using a VP-ITC MicroCalorimeter (GE Healthcare) at 295 K, and data were analyzed using the Origin ITC analysis software package. Titrations were always preceded by an initial injection of 3 μL and were carried out using sequential 10 μL injections with continuous stirring. The data were fitted to the "one binding site model" and apparent molar reaction enthalpy ($\Delta H^{\circ}$), apparent entropy ($\Delta S^{\circ}$), association constant ($K_A$), and binding stoichiometry ($N$) was determined.

## Analytical ultracentrifugation (AUC)

Sedimentation velocity (SV) experiments were performed using a Beckman Optima XL-I analytical centrifuge operated at a run temperature of 293K. Human MDGA1$_{ECTO}$ was concentrated to 60 μM (6.31 g/L) in TBS-CT buffer. Samples were held in Epon sector-shaped 2-channel centerpieces (6 mm path length) and were spun at 40,000 rpm. 200 sample distribution scans were taken incrementally, spaced 4 min apart. Data were collected using 280 nm absorbance optics.

Data were analyzed using the program Sedfit (Brown and Schuck, 2006). Scans 7-200 were used in the continuous c(s) distribution analysis. Analysis was performed with a floating frictional ratio and baseline, $S_{MIN} = 0.0$, $S_{MAX} = 20$, and a resolution value of 100. A value of 0.73 mL/g was used for the partial specific volumes. A buffer density value of 1.00527 g/cm$^3$ and buffer viscosity value of 0.01022 Poise was calculated using the Sednterp online application. Figures were prepared using the program GUSSI (Brautigam, 2015).

## Co-culture and immunocytochemistry

Constructs of the native, full-length (FL) human MDGA1 (Gln19-Arg955), and human MDGA2 (Gln21-Arg956), fused N-terminally with a HA epitope tag, and without C-terminal tags (yielding HA-MDGA1-2$_{FL}$), were cloned into the pHLsec vector (Aricescu et al., 2006b).

Constructs of the full-length human NL1 (–A ± B, –A ± B_Asn300Gln, ΔSite I, ΔSite II, ΔSite I+II, –A–B_Arg450Cys; Gln46-Val840), human NL2 (–A; Glu38-Val835), human NL3 (–A, –A_Arg451Cys; Gln38-Val848), and human NL4 (NL4(X); Gln42-Val816), fused N-terminally with a Myc epitope tag and fused C-terminally with ECFP (enhanced cyan fluorescent protein; yielding myc-NL1-4$_{FL}$), were cloned into the pHLsec vector (Aricescu et al., 2006b). NL1(–A–B)$_{FL}$_Arg450Cys and NL3(–A)$_{FL}$_Arg451Cys used native signal sequences and were not C-terminally fused to ECFP, to avoid the potential impact of these modifications on surface trafficking of the mutants.

Low density primary hippocampal cultures were prepared from E18 rat embryos as previously described (Kaech and Banker, 2006) and as approved by the University of British Columbia Animal Care Committee. Neuron cultures were maintained in Neurobasal (NB) medium (Thermo Fisher Scientific) supplemented with GlutaMAX-I (Thermo Fisher Scientific), B-27 supplement (Thermo Fisher Scientific) and 100 μM APV (Abcam). COS-7 cells were cultured in DMEM supplemented with 10% bovine growth serum and 100 I.U./mL penicillin-streptomycin. Cells were transfected using TransIT-LT1 transfection reagent (Mirus Bio) with (i) 0.5 μg myc-NL1-4$_{FL}$ and 1.1 μg HA-CD4, 1.1 μg HA-MDGA1$_{FL}$, or 1.6 μg HA-MDGA2$_{FL}$ for low ratio experiments; (ii) 0.5 μg myc-NL1-4$_{FL}$ and 1.75 μg HA-CD4, 1.75 μg HA-MDGA1$_{FL}$, or 2.5 μg HA-MDGA2$_{FL}$ for medium ratio experiments; and (iii) 0.5 μg myc-NL1-4$_{FL}$ and 2.5 μg

HA-CD4, 2.5 μg HA-MDGA1$_{FL}$, or 3.6 μg HA-MDGA2$_{FL}$ for high ratio experiments. HA-MDGA1$_{FL}$ and HA-MDGA2$_{FL}$ plasmid DNA amounts were adjusted to achieve similar surface protein levels. One day post-transfection, COS-7 cells were seeded onto 14 day in vitro (DIV) hippocampal cultures. After 20-24 hr the co-cultures were fixed in 4% paraformaldehyde (PFA) and 4% sucrose in PBS (pH 7.4) for 12 min at room temperature and incubated with blocking solution (3% bovine serum albumin, 5% normal goat serum in PBS) for 30 min at 310K. Surface NLs and MDGAs were labeled by incubating with anti-myc and anti-HA antibodies, respectively, for 1 hr at 310K. The cells were permeabilized with 0.2% Triton X-100 in PBS, blocked for 30 min at 310K and incubated with anti-synapsin1 and anti-tau antibodies overnight at 277K. Secondary antibodies were applied for 30 min at 310K and the coverslips were mounted onto glass slides with elvanol (Tris-HCl, glycerol, and polyvinyl alcohol with 2% 1,4-diazabi-cyclo[2,2,2]octane).

The following primary antibodies were used: rabbit polyclonal anti-c-*myc* (1:1000, Sigma), mouse monoclonal anti-HA (1:1000, IgG2b, clone 12CA5, Roche), mouse monoclonal anti-synapsin1 (1:8000, IgG1, clone 46.1, Synaptic Systems), mouse monoclonal anti-tau1 (1:4000, IgG2a, clone PC1C6, Millipore). The following secondary antibodies were used: goat AMCA-conjugated anti-rabbit (1:400, Jackson ImmunoResearch), goat Alexa Fluor 488-conjugated anti-mouse IgG2b (1:1000, Thermo Fisher Scientific), goat Alexa Fluor 568-conjugated anti-mouse IgG1 (1:1000, Thermo Fisher Scientific), goat Alexa Fluor 647-conjugated anti-mouse IgG2a (1:1000, Thermo Fisher Scientific).

### Image acquisition and analysis
Fluorescence microscopy was performed using a Zeiss Axioplan2 microscope. All images were acquired with a 63x oil immersion objective (NA 1.4) using MetaMorph imaging software (Molecular Devices). COS-7 cells with similar levels of both surface myc and HA were chosen for imaging and analysis for each co-culture experiment (Figure S6B). Image acquisition and analysis was performed with the experimenter blind to the experimental condition. Analysis was performed using NIH ImageJ software (Schneider et al., 2012). The total integrated intensity of punctate synapsin staining signal on a COS-7 cell was measured and normalized to the tau-positive axon contacting area. Cell surface levels of NLs and MDGAs were quantified by measuring mean intensity of myc and HA staining, respectively, on cells. Post-analysis images were adjusted for brightness and contrast across the entire image for presentation. Statistical analysis was performed using GraphPad Prism software. One-way ANOVA with post hoc Bonferroni multiple comparison test was used and statistical significance was set at $p < 0.05$. All data are presented as mean ± SEM from three independent experiments. Statistics are presented in Tables S3–S5.

### Surface expression of the NL3(–A) Arg451Cys mutant
Constructs of full-length (Gln38-Val848) wild-type human NL3(–A) and mutant NL3(–A) Arg451Cys, fused N-terminally to a Myc and V5 epitope tag, were cloned into the pCAGGS vector, generating pCAGGS-myc-V5-NL3(WT) and pCAGGS-myc-V5-NL3(R451C). Both constructs used native signal sequences and were not C-terminally fused to ECFP. Low density primary hippocampal cultures were prepared from E18 rat embryos as previously described (Kaech and Banker, 2006). Neuron cultures were maintained in Neurobasal (NB) medium (Thermo Fisher Scientific) supplemented with GlutaMAX-I (Thermo Fisher Scientific), B-27 supplement (Thermo Fisher Scientific) and 100 μM APV (Abcam). Cells were transfected by nucleofection using 2 μg of plasmid DNA and were then plated on coverglasses. After 3 days in vitro (DIV) the neurons were fixed in 4% paraformaldehyde (PFA) and 4% sucrose in PBS (pH 7.4) for 12 min at room temperature and incubated with blocking solution (3% bovine serum albumin, 5% normal goat serum in PBS) for 30 min at 310K. Surface NL3 was labeled by incubating with anti-V5 antibody overnight at 277K. The cells were permeabilized with 0.2% Triton X-100 in PBS, blocked for 30 min at 310K and incubated with anti-myc antibody overnight at 277K.

The following primary antibodies were used: rabbit polyclonal anti-c-*myc* (1:1000, Sigma) and mouse monoclonal anti-V5 (1:1000, IgG2a, Thermo Fisher). The following secondary antibodies were used: goat Alexa Fluor 488-conjugated anti-rabbit (1:1000, Thermo Fisher Scientific) and goat Alexa Fluor 647-conjugated anti-mouse IgG2a (1:1000, Thermo Fisher Scientific).

Fluorescence microscopy was performed using a Zeiss Axioplan2 microscope. All images were acquired using MetaMorph imaging software (Molecular Devices) and with a 10x air objective to capture the entire neuron in one field of view. The neurons were visualized using the 488 channel for myc and 647 channel for V5.

### Pulldown and mass spectrometry
Affinity chromatography was performed as previously described (Savas et al., 2014). Briefly, for each MDGA-Fc bait protein, five P21 rat brains were homogenized in homogenization buffer (4 mM HEPES, 0.32 M sucrose) with protease inhibitors using a glass Dounce homogenizer. Homogenates were centrifuged at 1,000 g for 15 min at 277 K. Supernatants were centrifuged again at 1000 g for 15 min. The resulting supernatants were then centrifuged at 10,000 g for 20 min. The pellet P2, containing crude synaptosomes, was resuspended in homogenization buffer and centrifuged at 10,000 g for 20 min, yielding pellet P2′ that contained washed crude synaptosomes. Pellet P2′ was extracted in 20 mM Tris pH 8.0, 0.1 mM CaCl$_2$ and 1% (w/v) Triton X-100 for 2 hr at 277 K. Extracts were centrifuged at 10,000 g for 30 min and the supernatants were diluted 1:1 with extraction buffer. Protein A beads (Pierce, 250 μL slurry) bound to 100 μg human Fc control protein or MDGA1-, MDGA1ΔIg1-3, or MDGA2-Fc proteins were added and rotated O/N at 277 K. Beads were packed into Poly-Prep chromatography columns (BioRad) and washed with 50 mL of high-salt wash buffer (50 mM HEPES pH 7.4, 300 mM NaCl, 0.1 mM CaCl$_2$, 5% glycerol and protease inhibitors), followed by a wash with 10 mL low-salt wash buffer (50 mM HEPES pH 7.4, 150 mM NaCl, 0.1 mM CaCl$_2$, 5% glycerol and protease inhibitors). Bound proteins were eluted from the beads by incubation with Pierce elution buffer and TCA precipitated overnight. For the MS analysis, we required

each protein to have two peptide matches and each peptide to have at least 1 tryptic terminus and an overall protein false discovery rate (FDR) < 1.2% for each dataset. Proteins shown in Figure S5B and Table S2 are the complete set of proteins found in both MDGA1- or MDGA2-Fc purifications after removing background proteins identified in Fc negative control purifications. Only proteins identified with two or more spectral counts were included in the analysis.

## DATA AND SOFTWARE AVAILABILITY

The accession number for the crystal structure of human NL1(–A+B)$_{ECTO}$ reported in this paper is PDB: 5OJK. The accession number for the crystal structure of chicken MDGA1$_{ECTO}$ reported in this paper is PDB: 5OJ2. The accession number for the crystal structure of the complex between human NL1(–A–B)$_{ECTO}$ and chicken MDGA1$_{ECTO}$ reported in this paper is PDB: 5OJ6.